Available online at www.sciencedirect.com
SCIENCE DIRECT®
Advances in Applied Mathematics 36 (2006) 213–250
ADVANCES IN Applied Mathematics
www.elsevier.com/locate/yaama

3PI algorithms for helical computer tomography ☆

Alexander Katsevich

Department of Mathematics, University of Central Florida, Orlando, FL 32816-1364

Received 4 June 2003; accepted 3 September 2005

Available online 17 February 2006

Abstract

Proposed are two theoretically exact convolution-based filtered backprojection inversion algorithms for helical computer tomography. An important feature of the algorithms is that they operate in the 3PI mode, which allows use of redundant data for the purpose of improving image quality. Results of a numerical experiment are presented.

1. Introduction

Helical computer tomography (CT) is a common imaging modality. Several approaches for exact image reconstruction in helical CT have been proposed. See e.g. [2,14] for the latest developments. Known exact algorithms can be classified into two groups: filtered backprojection (FBP) type and backprojection filtration (BPF) type. While BPF algorithms have improved significantly in the past few years [15,20,21,23], it still appears that they are much less efficient than their FBP counterparts. The main advantages of the BPF algorithms are flexibility with respect to source trajectory and ability to deal with some transverse data truncation. The FBP approach also allows one to handle different trajectories and tolerate some data truncation (see e.g. [17,19]), but the price to pay is a loss of computational efficiency. This is caused by the need to perform filtering along a two-parametric family of lines on the detector. The most efficient FBP algorithms are those where filtering is performed along a one-parametric family of lines [7,8,10,22]. Most of them operate in the 1PI mode [10] or close to the 1PI mode [22]. Let us recall briefly how the algorithm in [10] works. It can be numerically implemented in two steps. First, one performs shift-invariant filtering of the cone beam projections. Second, the result is back-projected in order

☆ This research was supported in part by NSF grant DMS-0104033 and Toshiba Medical Systems Corporation, Japan.
E-mail address: akatsevi@pegasus.cc.ucf.edu.

0196-8858/$ – see front matter
doi:10.1016/j.aam.2006.01.001

to form an image. At the backprojection step only the data within the Tam window (also known as 1PI window) are used. Recall that Tam window is obtained by projecting two turns of the helix adjacent to the current source position onto the detector plane. If the axial span of the detector array is large or if the pitch is small, this results in not using all the available data. However, studies have shown that increased detector usage leads to the reduction of motion and sampling artifacts, efficient use of the applied dose, etc. [3,11]. On the other hand, algorithms using larger detector area are computationally more intensive. A good compromise between the requirements of detector usage and computational efficiency are the so-called 3PI algorithms [16]. 3PI algorithms allow one to use the detector array which is about three times as large as that required for 1PI algorithms. Two 3PI algorithms have been proposed in [4,16]. These algorithms are based on different approximations and are not exact. A more recent approximate algorithm, which can incorporate an arbitrary amount of redundant data, has been proposed in [12]. In this paper we propose two exact and efficient convolution-based FBP algorithms, which operate in the 3PI mode.

The paper is organized as follows. In Section 2 we review a general cone-beam inversion formula obtained in [9]. This formula is based on a weight function n. In order to transform this formula to a shift-invariant FBP algorithm for helical CT, that would also solve the long object problem and use axially-truncated projections, one has to find an appropriate weighting function n. In Section 3 we discuss 3PI lines and their properties. In Sections 4 and 5 we develop a theory, which in Section 6 allows us to find the required n. In Section 7 we derive from n the first reconstruction algorithm. In Section 8 we propose another weighting function n_{new} and derive from it an improved reconstruction algorithm, which is more efficient and provides much better detector utilization. Results of a numerical experiment are presented in Section 9. Some auxiliary results are proven in Section 10.

2. Theoretical background

First we introduce the necessary notations. Let

$$C := \bigl\{y \in \mathbb{R}^3\colon\ y_1 = R\cos(s),\, y_2 = R\sin(s),\, y_3 = s(h/2\pi),\, s \in \mathbb{R}\bigr\}, \tag{2.1}$$

where $h > 0$, be a helix, and U be an open set strictly inside the helix:

$$\overline{U} \subset \bigl\{x \in \mathbb{R}^3\colon\ x_1^2 + x_2^2 < r^2\bigr\}, \quad 0 < r < R, \tag{2.2}$$

S^2 is the unit sphere in $\mathbb{R}^3$, and

$$D_f(y,\beta) := \int_0^\infty f(y+\beta t)\,dt, \quad \beta \in S^2, \tag{2.3}$$

$$\beta(s,x) := \frac{x - y(s)}{|x - y(s)|}, \quad x \in U,\ s \in \mathbb{R}, \qquad \Pi(x,\xi) := \bigl\{y \in \mathbb{R}^3\colon\ (y-x)\cdot\xi = 0\bigr\}, \tag{2.4}$$

that is $D_f(y,\beta)$ is the cone beam transform of f. Given $(x,\xi) \in U \times (\mathbb{R}^3 \setminus 0)$, let $s_j = s_j(\xi, \xi\cdot x)$, $j = 1, 2, \ldots$, denote points of intersection of the plane $\Pi(x,\xi)$ with C. Also, $\dot{y}(s) := dy/ds$. For $\beta \in S^2$, $\beta^\perp$ denotes the great circle $\{\alpha \in S^2\colon\ \alpha\cdot\beta = 0\}$.

Fix any $x \in U$, where f needs to be computed. In order to compute $f(x)$ we use a section of the helix of finite extent, which is to be determined later. For now it is denoted $C(x)$. The corresponding parametric interval is denoted $I(x)$. Introduce the sets

$$\begin{aligned} Crit(s,x) &:= \big\{\alpha \in \beta^{\perp}(s,x):\ \Pi(x,\alpha) \text{ is tangent to } C(x) \text{ or} \\ &\qquad\qquad \Pi(x,\alpha) \text{ contains an endpoint of } C(x)\big\}, \\ I_{\mathrm{reg}}(x) &:= \big\{s \in I:\ Crit(s,x) \subsetneq \beta^{\perp}(s,x)\big\}, \\ Crit(x) &:= \bigcup_{s\in I} Crit(s,x). \end{aligned} \tag{2.5}$$

Sometimes $Crit(s,x)$ coincides with $\beta^{\perp}(s,x)$. This happens, for example, if $\beta(s,x)$ is parallel to $\dot{y}(s)$ or the line through $y(s) \in C(x)$ and x contains an endpoint of $C(x)$. $I_{\mathrm{reg}}(x)$ is open. As is well known (see [1, Proposition 0.28]), the set $Crit(x)$ has Lebesgue measure zero.

The assumptions about $C(x)$ are the following.

Property C1 *((Completeness condition)). Any plane through x intersects $C(x)$ at least at one point.*

Property C2. *The number of directions in $Crit(s,x)$ is uniformly bounded on $I_{\mathrm{reg}}(x)$.*

Property C3. *The number of points in $\Pi(x,\alpha) \cap C$ is uniformly bounded on $S^2 \setminus Crit(x)$.*

Property C1 is the most important from the practical point of view. Note that it is slightly weaker than Tuy's condition, because we do not require that every plane through x intersects $C(x)$ at least once in a non-tangential way. Properties C2 and C3 merely state that the curve $C(x)$ is not too exotic.

An important ingredient in the construction of the inversion formula is weight function $n(s,x,\alpha)$, $s \in I_{\mathrm{reg}}(x)$, $\alpha \in \beta^{\perp}(s,x) \setminus Crit(s,x)$. The function n can be understood as follows. x and α determine the plane $\Pi(x,\alpha)$, and the weight n assigned to $y(s) \in \Pi(x,\alpha) \cap C(x)$ depends on the location of x. In view of this interpretation we assume $n(s,x,\alpha) = n(s,x,-\alpha)$. The main assumptions about n are the following.

Property W1. *Normalization condition*:

$$\sum_j n(s_j,x,\alpha) = 1, \quad \alpha \in S^2 \setminus Crit(s,x). \tag{2.6}$$

In (2.6) and throughout the paper $\sum_j$ denotes the sum over all s_j such that $y(s_j) \in C(x) \cap \Pi(x,\alpha)$.

Property W2. *There exist finitely many C^1 functions $\alpha_k(s,x) \in \beta^{\perp}(s,x)$, $s \in I_{\mathrm{reg}}(x)$, such that $n(s,x,\alpha)$ is locally constant in a neighborhood of any (s,α), where $s \in I_{\mathrm{reg}}(x)$ and $\alpha \in \beta^{\perp}(s,x)$, $\alpha \notin (\bigcup_k \alpha_k(s,x)) \cup Crit(s,x)$.*

Denote

$$\begin{aligned}&\phi(s,x,\theta) := \operatorname{sgn}\big(\alpha\cdot\dot{y}(s)\big)n(s,x,\alpha),\quad \alpha=\alpha(s,x,\theta)\in\beta^{\perp}(s,x),\\ &\alpha^{\perp}(s,x,\theta) := \frac{\partial}{\partial\theta}\alpha(s,x,\theta)=\beta(s,x)\times\alpha(s,x,\theta).\end{aligned}\tag{2.7}$$

Here θ is the polar angle in the plane $\beta^{\perp}(s,x)$. Under assumptions C1–C3, W1, and W2 the following general inversion formula is derived in [9]:

$$\begin{aligned}f(x) = -\frac{1}{4\pi^2}\int\limits_{I(x)}\sum_{m=1}^{M(s,x)}\frac{c_m(s,x)}{|x-y(s)|}\\ \times\int\limits_0^{2\pi}\frac{\partial}{\partial q}D_f\big(y(q),\cos\gamma\beta(s,x)+\sin\gamma\alpha^{\perp}(s,x,\theta_m)\big)\big|_{q=s}\frac{d\gamma}{\sin\gamma}\,ds,\end{aligned}\tag{2.8}$$

where $\theta_m\in[0,\pi)$, $m=1,\dots,M(s,x)$, are the points where $\phi(s,x,\theta)$ is discontinuous, and $c_m(s,x)$ are values of the jumps:

$$c_m(s,x) := \lim_{\epsilon\to 0^+}\big(\phi(s,x,\theta_m+\epsilon)-\phi(s,x,\theta_m-\epsilon)\big).\tag{2.9}$$

Unless n is chosen appropriately, the inversion formula is not necessarily of the FBP type.

3. Properties of 3PI lines

The following facts are established in this section:

- It is proven that each $x\in U$ has either one or three 3PI lines (this fact was also established in [16]);
- An explicit equation for the boundary between the two cases is obtained. Inside the boundary each x has only one 3PI line, while outside each x has three 3PI lines;
- A result is derived, which allows one to construct a simple and stable algorithm for finding the 3PI line (or, lines) for each $x\in U$;
- A relationship between the endpoints of the 3PI lines of x is established;
- The notions of 3PI window, 3PI parametric interval of x, and 3PI helical segment of x are introduced.

Suppose that the x-ray source is fixed at $y(s_0)$ for some $s_0\in\mathbb{R}$. Since the detector array rotates together with the source, the detector plane depends on s_0 and is denoted $DP(s_0)$. It is assumed that $DP(s_0)$ is parallel to the axis of the helix and is tangent to the cylinder $y_1^2+y_2^2=R^2$ (cf. (2.1)) at the point opposite to the source. Thus, the distance between $y(s_0)$ and the detector plane is $2R$ (see Fig. 1). Introduce coordinates in the detector plane as follows. Let the d_1-axis be perpendicular to the axis of the helix, the d_2-axis be parallel to it, and the origin coincide with

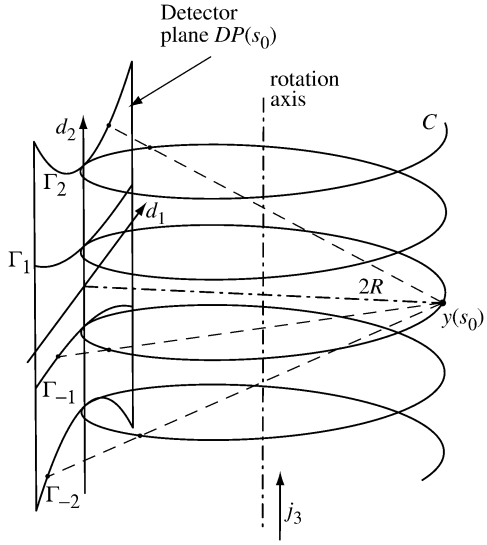

Fig. 1. Stereographic projection of the helix onto the detector plane.

the projection of $y(s_0)$. Project stereographically the upper and lower turns of the helix onto the detector plane as shown in Fig. 1. This gives the following parametric curves:

$$\begin{aligned} &d_1(s) = 2R\frac{\sin(s-s_0)}{1-\cos(s-s_0)}, \qquad d_2(s) = \frac{h}{\pi}\frac{s-s_0}{1-\cos(s-s_0)}, \\ &\rho + 2\pi(j-1) \leqslant s - s_0 \leqslant 2\pi j - \rho, \quad j \geqslant 1, \quad \text{or} \\ &\rho + 2\pi j \leqslant s - s_0 \leqslant 2\pi(j+1) - \rho, \quad j \leqslant -1, \end{aligned} \tag{3.1}$$

where ρ is determined by radius of support of the patient: $\rho = 2\cos^{-1}(r/R)$ (cf. (2.2)). These curves are denoted Γ_j, $j = \pm 1, \pm 2, \ldots$ (see Fig. 2). Let $\hat{x}$ denote the projection of x. As is well known, $\hat{x}$ is between Γ_{-1} and Γ_1 if and only if $s_0 \in I^{1\mathrm{PI}}(x)$. Here $I^{1\mathrm{PI}}(x) := [b^{1\mathrm{PI}}(x), t^{1\mathrm{PI}}(x)]$ is the 1PI parametric interval of x. Equations (3.1) imply that the curves Γ_j are strictly convex. Also, Γ_1 approaches L_0 from above as $s \to s_0^+$ (in this case $d_1(s) \to +\infty$), Γ_{-1} approaches L_0 from below as $s \to s_0^-$ ($d_1(s) \to -\infty$). L_0 denotes the projection of the helical tangent onto the detector plane. Note that if two neighboring Γ curves are intersected by a vertical line (i.e., parallel to the d_2-axis), then the difference between values of the parameter s at the two points of intersection is exactly 2π. The region on the detector bounded by Γ_{-1} and Γ_1 is known in the literature as 1PI or Tam–Danielsson window [5,18].

Connect an arbitrary source position $y(s_0)$ to all points $y(s)$ on the helix, where

$$2\pi < s - s_0 < 4\pi \quad \text{or} \quad -4\pi < s - s_0 < -2\pi. \tag{3.2}$$

This gives two surfaces, which are denoted $S_U^{3\mathrm{PI}}(s_0)$ and $S_L^{3\mathrm{PI}}(s_0)$. The region bounded by the two surfaces and the cylinder $x_1^2 + x_2^2 = R^2$ is denoted $V^{3\mathrm{PI}}(s_0)$. Later we will also need $V^{1\mathrm{PI}}(s_0)$, which is constructed in a similar fashion by connecting $y(s_0)$ to the adjacent turns of the helix: $0 < |s - s_0| < 2\pi$. Let x be fixed. If s_0 is sufficiently small, then $S_U^{3\mathrm{PI}}(s_0)$ is below x.

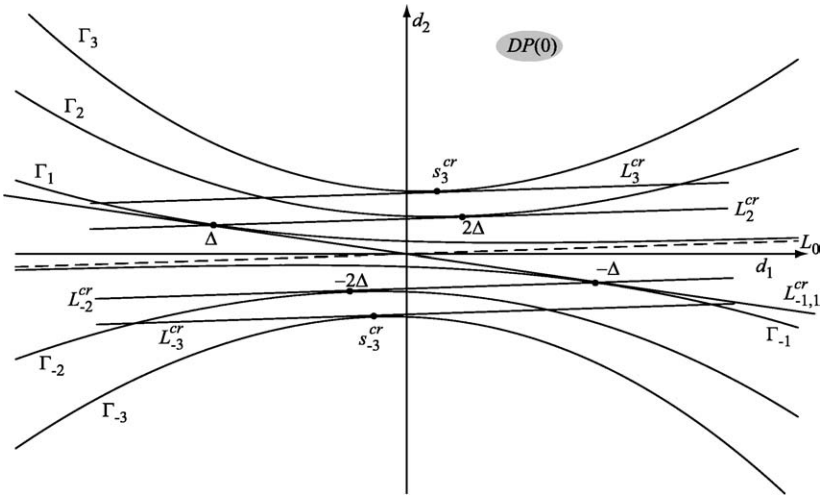

Fig. 2. Detector plane with various projections and important lines shown.

As s_0 increases, two cases are possible (cf. [16]). In the first one, known as continuous illumination, x enters $V^{3\mathrm{PI}}(s_0)$ through $S_U^{3\mathrm{PI}}(s_0)$ and leaves $V^{3\mathrm{PI}}(s_0)$ through $S_L^{3\mathrm{PI}}(s_0)$. Clearly, the above procedure yields a unique 3PI interval $[b_0(x), t_0(x)]$ and the corresponding unique 3PI line $L_0^{3\mathrm{PI}}(x)$. In the second case, known as interrupted illumination, x enters and leaves $V^{3\mathrm{PI}}(s_0)$ several times. More precisely, x intersects each of the surfaces $S_U^{3\mathrm{PI}}(s_0)$ and $S_L^{3\mathrm{PI}}(s_0)$ exactly three times. Therefore, the above procedure now gives three 3PI lines $L_i^{3\mathrm{PI}}(x)$, $i = 1, 2, 3$. The corresponding values of the parameter are denoted $b_i(x)$, $t_i(x)$, $i = 1, 2, 3$. Due to the symmetry of the helix, if x leaves (enters) $V^{3\mathrm{PI}}(s_0)$ when $s_0 = b_i(x)$, then x enters (leaves) $V^{3\mathrm{PI}}(s_0)$ when $s_0 = t_i(x)$, $i = 1, 2, 3$.

We now prove that only these two cases are possible. To simplify the derivations we may assume without loss of generality that $R = 1$ and $h = 2\pi$ in (2.1). Because of the symmetry, it is sufficient to consider only points within the plane $x_3 = 0$ and rotate $S_L^{3\mathrm{PI}}(s_0)$ over the interval $0 < s_0 < 4\pi$. Equivalently, we can fix the source at $s_0 = 0$ and rotate the disk $\{(x_1, x_2, x_3) \in \mathbb{R}^3\colon\ x_1^2 + x_2^2 < 1, x_3 = 0\}$ according to

$$x_1(\varphi) = r\cos(\varphi - \varphi_0), \qquad x_2(\varphi) = -r\sin(\varphi - \varphi_0), \qquad x_3(\varphi) = -\varphi, \quad 0 \leqslant \varphi < 4\pi, \tag{3.3}$$

where $0 \leqslant r < 1$. Thus, if $\varphi = 0$, we fix a point $x(0) = (r\cos(\varphi_0), r\sin(\varphi_0), 0)$ and then observe how it spirals down in the clockwise direction. Our goal is to find a boundary of the region where the number of intersection points with $S_L^{3\mathrm{PI}}(0)$ changes. Obviously, $x(0)$ belongs to the boundary if $x(\varphi) \in S_L^{3\mathrm{PI}}(0)$ and $\dot{x}(\varphi)$ is tangent to $S_L^{3\mathrm{PI}}(0)$. Parametric equations of $S_L^{3\mathrm{PI}}(0)$ are

$$\big(1 + \lambda(\cos s - 1), \lambda\sin s, \lambda s\big), \quad 0 < \lambda < 1,\ -4\pi < s < -2\pi, \tag{3.4}$$

so the above two conditions become

$$r\cos(\varphi - \varphi_0) = 1 + \lambda(\cos s - 1), \qquad -r\sin(\varphi - \varphi_0) = \lambda\sin s, \quad -\varphi = \lambda s; \tag{3.5}$$

$$\big(-r\sin(\varphi-\varphi_0), -r\cos(\varphi-\varphi_0), -1\big)\cdot\big[(\cos s-1, \sin s, s)\times(-\sin s, \cos s, 1)\big]=0, \quad (3.6)$$

where we have used that $\lambda\neq 0$. Substitution of the first two equations in (3.5) into (3.6) gives

$$\lambda\sin s(\sin s - s\cos s) + \big(1+\lambda(\cos s-1)\big)\cdot(s\sin s+\cos s-1) - (1-\cos s)=0. \quad (3.7)$$

(3.7) reduces to

$$(\lambda-1)\big(2(1-\cos s) - s\sin s\big)=0. \quad (3.8)$$

Since $\lambda\neq 1$, the only solution to (3.8) is $s=-2\Delta$, where $\Delta\approx 1.43\pi$ satisfies

$$\tan(\Delta)=\Delta, \quad \Delta\in(\pi,2\pi). \quad (3.9)$$

Substitution into (3.5) gives

$$x_1(\varphi)=1+\lambda\big(\cos(2\Delta)-1\big), \qquad x_2(\varphi)=-\lambda\sin(2\Delta), \quad \varphi=2\lambda\Delta,\ 0<\lambda<1. \quad (3.10)$$

Or, alternatively, from (3.3):

$$x(\varphi)=(1-\lambda)(1,0,0)+\lambda\big(\cos(-2\Delta), \sin(-2\Delta), -2\Delta\big), \quad 0<\lambda<1. \quad (3.11)$$

Rotating back to the plane $x_3=0$ gives the parametric curve

$$\begin{aligned} x_1^b(\lambda) &= r\cos(\varphi_0)=\cos(2\lambda\Delta)\big(1+\lambda\big(\cos(2\Delta)-1\big)\big)+\sin(2\lambda\Delta)\lambda\sin(2\Delta)\\ &= (1-\lambda)\cos(2\lambda\Delta)+\lambda\cos\big(2\Delta(\lambda-1)\big),\\ x_2^b(\lambda) &= r\sin(\varphi_0)=\sin(2\lambda\Delta)\big(1+\lambda\big(\cos(2\Delta)-1\big)\big)-\cos(2\lambda\Delta)\lambda\sin(2\Delta)\\ &= (1-\lambda)\sin(2\lambda\Delta)+\lambda\sin\big(2\Delta(\lambda-1)\big),\\ &0<\lambda<1. \end{aligned} \quad (3.12)$$

Since $0=(1-\lambda)(2\lambda\Delta)+\lambda(2\Delta(\lambda-1))$, (3.13) implies that x belongs to the boundary between one- and three-3PI line regions if and only if x belongs to a line segment connecting two points on the helix that are 2Δ away from each other.

Note that

$$x_1^b(\lambda=0)=x_1^b(\lambda=1)=1, \qquad x_2^b(\lambda=0)=x_2^b(\lambda=1)=0. \quad (3.13)$$

Thus, (3.13) is a closed curve. The graph of (3.13) is a heart-shaped curve shown in Fig. 3. We see that the curve has no self intersections, so it divides the open disk $x_1^2+x_2^2<1$ into two regions: X_1 and X_3. In the central one, denoted X_1, there is one 3PI line for each x. In the exterior one, denoted X_3, there are three 3PI lines for each x. These facts can be verified, for example, numerically by analyzing one point from each region (this was done in [16]). An analytical proof is given below. Our argument implies also the uniqueness of the 3PI lines. Suppose two 3PI lines intersect at a point x. By considering rotating volume $V^{3\mathrm{PI}}(s_0)$ we conclude that there is necessarily a third 3PI line through x. Consequently, $x\in X_3$, and no more 3PI lines through x can exist.

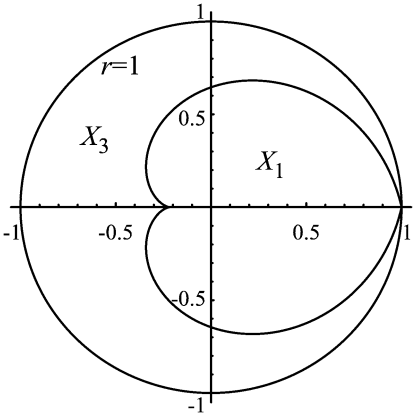

Fig. 3. The curves $(x_1^b(\lambda), x_2^b(\lambda))$, $\lambda \in [0, 1]$, and $r = 1$.

A derivation somewhat similar to (3.3)–(3.7) is contained in [16]. However, in [16] the equation of the boundary curve is obtained in an implicit form. This makes it difficult to study the curve theoretically. Here the curve is described by explicit parametric equations (3.13).

Quantity Δ, which is introduced in (3.9), is featured prominently on the detector plane. Let L_j^{cr} be the line tangent to Γ_j and parallel to the helical tangent (see Fig. 2). Then the point where L_2^{cr} is tangent to Γ_2 is 2Δ. Let $L_{-1,1}^{\mathrm{cr}}$ be the line tangent to Γ_{-1} and Γ_1. Then the points of tangency are $-\Delta$ and Δ, respectively. Moreover, $L_{-1,1}^{\mathrm{cr}}$ and L_2^{cr} intersect precisely at the point $\Delta \in \Gamma_1$.

Following [6], the three equations in (3.5) can be combined into one. Solving the first two equations in (3.5) for λ and s, we get

$$\begin{aligned} \lambda(\theta) &= 1 - \frac{1}{2}\frac{1-r^2}{1-r\cos\theta}, \\ \tan(s/2) &= \frac{1-r\cos\theta}{r\sin\theta}, \quad s = s(\theta) \in (-4\pi, -2\pi),\ \theta := \varphi_0 - \varphi. \end{aligned} \tag{3.14}$$

Substitution into the third one gives an equation for finding the 3PI lines

$$\Phi(\theta) := \lambda(\theta)s(\theta) - \theta = -\varphi_0, \quad \theta \in (\varphi_0 - 4\pi, \varphi_0). \tag{3.15}$$

Once θ is determined, we easily find $s(\theta)$ and $\varphi = \varphi_0 - \theta$. The corresponding 3PI line is obtained by rotating the line containing $y(0), y(s(\theta))$ through the angle φ. To study how many solutions (3.15) has, we can restrict θ to any interval of length 4π, for example $[0, 4\pi]$. Up to a positive factor the derivative of Φ is given by

$$\Phi'(\theta) \sim r\sin\theta \tan^{-1}\left(\frac{1-r\cos\theta}{r\sin\theta}\right) - (1 - r\cos\theta). \tag{3.16}$$

Thus the critical points of Φ can be found from

$$\tan^{-1}\left(\frac{1-r\cos\theta}{r\sin\theta}\right) = \frac{1-r\cos\theta}{r\sin\theta}. \tag{3.17}$$

Since the range of $\tan^{-1}$ is $(-2\pi, -\pi)$ (cf. (3.14)), we get

$$\frac{1 - r\cos\theta}{r\sin\theta} = -\Delta. \tag{3.18}$$

If we determine θ_0 from

$$(\cos\theta_0, \sin\theta_0) = \left(\frac{1}{\sqrt{1+\Delta^2}}, -\frac{\Delta}{\sqrt{1+\Delta^2}}\right), \quad \theta_0 \in (0, 2\pi), \tag{3.19}$$

(3.18) becomes

$$\cos(\theta - \theta_0) = \left[r\sqrt{1+\Delta^2}\right]^{-1}. \tag{3.20}$$

This confirms that if $r < r_0 := (1 + \Delta^2)^{-1/2} \approx 0.217$, then $\Phi(\theta)$ is monotone and only one solution to (3.15) exists (see Fig. 4). Consequently, only one 3PI line is possible. If $r = r_0$, there are two critical points on the interval $[0, 4\pi]$:

$$\theta_1 = \theta_0, \qquad \theta_2 = \theta_1 + 2\pi. \tag{3.21}$$

Since $\Phi'(0), \Phi'(2\pi), \Phi'(4\pi) < 0$, Φ is decreasing, and again only one solution exists. Suppose $r > r_0$. Now there are four critical points:

$$\begin{aligned} \theta_1 &= \theta_0 - \cos^{-1}\left(\left[r\sqrt{1+\Delta^2}\right]^{-1}\right), \quad \theta_3 = \theta_1 + 2\pi, \\ \theta_2 &= \theta_0 + \cos^{-1}\left(\left[r\sqrt{1+\Delta^2}\right]^{-1}\right), \quad \theta_4 = \theta_2 + 2\pi. \end{aligned} \tag{3.22}$$

The assumption $r_0 < r < 1$ implies $0 < \theta_1 < \theta_2 < \theta_3 < \theta_4 < 4\pi$. Elementary analysis shows that $\Phi'(\theta) < 0$ on $[0, \theta_1), (\theta_2, \theta_3), (\theta_4, 4\pi]$, $\Phi'(\theta) > 0$ on $(\theta_1, \theta_2), (\theta_3, \theta_4)$, and $\Phi(\theta_4) < \Phi(\theta_1)$ (see Fig. 5). Consequently, either one or three solutions are possible. This analysis can also be used in a numerical algorithm for finding 3PI lines.

To find out the relationship between $b_i(x), t_i(x)$, $x \in X_3$, consider how x enters and leaves $V^{3\mathrm{PI}}(s_0)$. For simplicity of notation we will omit the argument x from b_i, t_i. Because of symmetry, x intersects each of the surfaces $S_U^{3\mathrm{PI}}(s_0)$ and $S_L^{3\mathrm{PI}}(s_0)$ equal number of times. Since

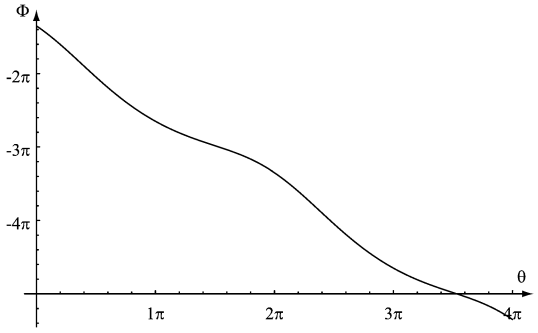

Fig. 4. The graph of $\Phi(\theta)$ for $r = 0.1$.

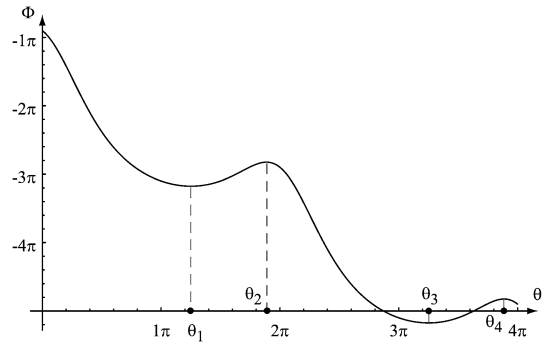

Fig. 5. The graph of $\Phi(\theta)$ for $r = 0.4$.

$V^{1\mathrm{PI}}(s_0) \subset V^{3\mathrm{PI}}(s_0)$ and the 1PI segment of x is unique, intersections of x with $S_L^{3\mathrm{PI}}(s_0)$ follow after the intersections of x with $S_U^{3\mathrm{PI}}(s_0)$. Therefore,

$$b_1 < b_2 < b_3 < t_1. \tag{3.23}$$

Considering the projection of the helix onto the x_1x_2-plane, we conclude

$$b_2 > b_1 \quad \Rightarrow \quad t_2 > t_1,\ b_3 > b_2 \quad \Rightarrow \quad t_3 > t_2. \tag{3.24}$$

Combining (3.23) and (3.24) gives

$$b_1 < b_2 < b_3 < t_1 < t_2 < t_3. \tag{3.25}$$

Since x enters $V^{3\mathrm{PI}}(s_0)$ for the first time when $s_0 = b_1$, then x leaves $V^{3\mathrm{PI}}(s_0)$ when $s_0 = b_2$. Continuing this argument for each of the values in (3.25) we conclude

$$\begin{aligned} x \in V^{3\mathrm{PI}}(s_0) \quad &\Leftrightarrow \quad s_0 \in I^{3\mathrm{PI}}(x) := [b_1, b_2] \cup [b_3, t_1] \cup [t_2, t_3], \\ &\quad 2\pi < t_i - b_i < 4\pi, \quad i = 1, 2, 3. \end{aligned} \tag{3.26}$$

In terms of the detector plane (3.26) implies that $\hat{x}$ is between Γ_2 and Γ_{-2} on $DP(s_0)$ if and only if $s_0 \in I^{3\mathrm{PI}}(x)$. Therefore, using the analogy with the 1PI case, we call this region the 3PI window. Continuing the analogy, $I^{3\mathrm{PI}}(x)$ is called the 3PI parametric interval of x, and $C^{3\mathrm{PI}}(x) := \{y(s) \in C\colon\ s \in I^{3\mathrm{PI}}(x)\}$ is called the 3PI helical segment of x.

By construction, $V^{1\mathrm{PI}}(s_0) \subset V^{3\mathrm{PI}}(s_0)$. Consequently, $[b^{1\mathrm{PI}}, t^{1\mathrm{PI}}] \subset (b_i, t_i)$, $i = 1, 2, 3$, so

$$\left[b^{1\mathrm{PI}}, t^{1\mathrm{PI}}\right] \subset (b_3, t_1). \tag{3.27}$$

4. Intersections of planes through x with $C^{3\mathrm{PI}}(x)$

As follows from the general approach given in Section 2, in order to obtain an inversion formula one has to specify (1) a section of trajectory, which will be used for image reconstruction at each $x \in U$, and (2) a normalized weight function n. The first item is easy. We will use $C^{3\mathrm{PI}}(x)$, the 3PI helical segment of x. To construct the appropriate n is much more difficult. This will be done in Section 6. Here we make a preliminary step in that direction. In order to come up with

Table 1
Numbers of intersection points within the parametric intervals

Parametric interval	(b_1, b_2)	(b_2, b_3)	(b_3, t_1)	(t_1, t_2)	(t_2, t_3)
Number of intersection points with the interval	m_1	m_2	m_3	m_4	m_5

an FBP algorithm, the function ϕ defined by (2.7) must be continuous in a neighborhood of all planes containing 3PI lines of x. Since $n(s, x, \alpha)$ depends on the number of intersection points (IPs) in $\Pi(x, \alpha) \cap C^{3\mathrm{PI}}(x)$, in this section we study what happens with the IPs when a rotating plane through x and $y(s) \in C^{3\mathrm{PI}}(x)$ passes through a 3PI line of x.

First consider how a generic plane $\Pi \ni x$ intersects $C^{3\mathrm{PI}}(x)$. Here we assume that Π does not contain the 3PI line (or, any of the 3PI lines) of x. If $x \in X_1$, the number of IPs is odd. Suppose now $x \in X_3$. Define the variables m_j according to Table 1.

In view of (3.26) we would like to show that $m_1 + m_3 + m_5$ is odd. By construction,

$$\begin{aligned} m_1 + m_2 + m_3 &= 2k_1 + 1, \\ m_2 + m_3 + m_4 &= 2k_2 + 1, \\ m_3 + m_4 + m_5 &= 2k_3 + 1. \end{aligned} \tag{4.1}$$

By adding the equations and rearranging the terms, the desired assertion follows:

$$m_1 + m_3 + m_5 = 2(k_1 + k_2 + k_3 - m_2 - m_3 - m_4) + 3. \tag{4.2}$$

Now we consider how the number of IPs might change. Pick any plane $\Pi_0 \ni y(b_i), y(t_i)$, and let α_0 be a unit vector perpendicular to Π_0. Let $y(s) \in C^{3\mathrm{PI}}(x) \cap \Pi_0$, $s \neq b_i, t_i$. Clearly, $\alpha_0 \in \beta^{\perp}(s, x)$. Two cases are possible.

Case I. Locally, the sections of $C^{3\mathrm{PI}}(x)$ attached to $y(b_i)$ and $y(t_i)$, respectively, are on different sides of Π_0.

Case II. Locally, the sections of $C^{3\mathrm{PI}}(x)$ attached to $y(b_i)$ and $y(t_i)$, respectively, are on the same side of Π_0.

In Case I a small rotation of $\Pi(x, \alpha)$, $\alpha \in \beta^{\perp}(s, x)$, across $\alpha = \alpha_0$ changes the number of points in $\Pi(x, \alpha) \cap C^{3\mathrm{PI}}(x)$ by two. In Case II the number of IPs stays the same. Moreover, the same case takes place for all other $y(s) \in C^{3\mathrm{PI}}(x) \cap \Pi_0$. This argument can be reversed. Fix $s \in I^{3\mathrm{PI}}(x)$. Let Π_0 be the plane through $y(s)$, $y(b_i)$, and $y(t_i)$, and α_0 be a unit vector perpendicular to Π_0. If a small rotation $\Pi(x, \alpha)$, $\alpha \in \beta^{\perp}(s, x)$, changes the number of points in $\Pi(x, \alpha) \cap C^{3\mathrm{PI}}(x)$ by two, then Case I takes place. If the number of IPs stays the same, Case II occurs.

If $x \in X_1$, in Case I a small rotation of $\Pi(x, \alpha)$, $\alpha \in \beta^{\perp}(s, x)$, across $\alpha = \alpha_0$ results in the birth (or, disappearance) of a pair of points, which are located in an immediate neighborhood of the edges of $I^{3\mathrm{PI}}(x)$ (see Fig. 6, left panel). In Case II an IP located near an edge of $I^{3\mathrm{PI}}(x)$ jumps to another edge (see Fig. 6, right panel). If $x \in X_3$, the situation is similar. Note, however, that the locations of the newly born (or, disappearing) points is next to the endpoints of the 3PI line, across which $\Pi(x, \alpha)$ is passing (see Fig. 7).

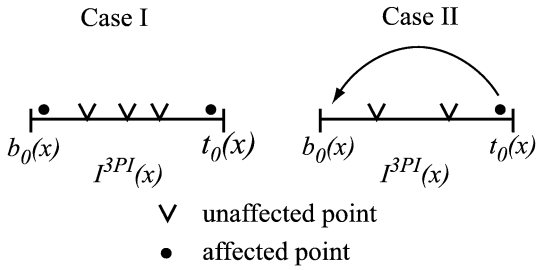

Fig. 6. Illustration of what happens with intersection points when $x \in X_1$ and $\Pi(x, \alpha)$ passes through $L_0^{3\mathrm{PI}}(x)$.

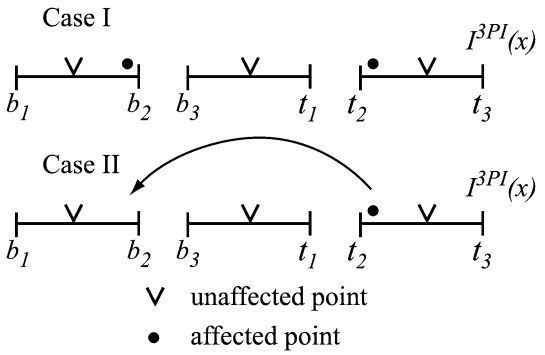

Fig. 7. Illustration of what happens with intersection points when $x \in X_3$ and $\Pi(x, \alpha)$ passes through $L_2^{3\mathrm{PI}}(x)$.

5. An auxiliary construction

As was mentioned in Section 4, in order to obtain the weight function n with good properties we have to investigate what happens with the IPs in $\Pi(x, \alpha) \cap C^{3\mathrm{PI}}(x)$ for all α. In particular, we have to know how many IPs there are, how they are distributed over $I^{3\mathrm{PI}}(x)$, and how it can happen that the number of IPs changes. In this section we come up with a convenient geometrical construction, which allows us to easily visualize the answers to all these questions.

Suppose first that continuous illumination takes place. Consider the following two curves on the surface of the unit sphere S^2. The first curve consists of all unit vectors α orthogonal to $L^{3\mathrm{PI}}(x)$ and is denoted by A. The other curve consists of vectors

$$\alpha(s) = \pm \frac{(x - y(s)) \times \dot{y}(s)}{|(x - y(s)) \times \dot{y}(s)|}, \quad s \in I^{3\mathrm{PI}}(x), \tag{5.1}$$

and is denoted by T. For each s, $\alpha(s)$ is a unit vector perpendicular to the plane which passes through x and is tangent to C at $y(s)$. It is not convenient to represent these curves directly on S^2, so they will be shown on the plane using spherical coordinates (θ_1, θ_2) defined by

$$S^2 \ni \alpha(s) = (\cos\theta_1 \sin\theta_2, \sin\theta_1 \sin\theta_2, \cos\theta_2), \quad -\pi \leqslant \theta_1 \leqslant \pi,\ 0 \leqslant \theta_2 < \pi. \tag{5.2}$$

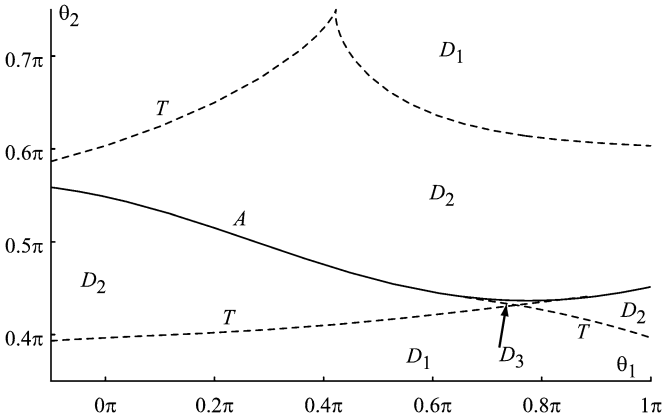

Fig. 8. The continuous illumination case, $x = (0, 0.25, 0)$.

Table 2
The continuous illumination case. Number of intersection points within $I^{3\mathrm{PI}}(x)$, $x = (0, 0.25, 0)$, for various domains

Domain	D_1	D_2	D_3
Number of intersection points inside $I^{3\mathrm{PI}}(x)$	1	3	5

Since both α and $-\alpha$ define the same plane, we can restrict θ_1 to any interval of length π and "glue" the opposite boundaries using the identification

$$(\theta_1, \theta_2) \cong \big((\theta_1 + \pi)_{\mathrm{mod}\, 2\pi}, \pi - \theta_2\big). \tag{5.3}$$

A typical situation for $x = (0, 0.25, 0)$ is shown in Fig. 8. It is very convenient to think about points on S^2 not only as unit vectors, but also as planes. Each $\alpha \in S^2$ corresponds to a unique plane through x with normal vector α. This correspondence is one-to-one if vectors with opposite orientation are identified.

Consider curves A and T in more detail. Obviously, T starts and ends on A. The endpoints of T correspond to the planes that contain $L^{3\mathrm{PI}}(x)$ and are tangent to $C^{3\mathrm{PI}}(x)$ at $y(b_0)$ or $y(t_0)$. T does not intersect A at any other point $s_0 \in (b_0, t_0)$. Indeed, suppose such a point exists. Consider the stereographic projection of the helix and $L^{3\mathrm{PI}}(x)$ from $y(s_0)$. Since $b_0 < s_0$, the projection of $y(b_0)$ is below L_0. Similarly, the projection of $y(t_0)$ is above L_0. By assumption, the slope of $\hat{L}^{3\mathrm{PI}}(x)$ (which is the projection of $L^{3\mathrm{PI}}(x)$ onto $DP(s_0)$) is the same as the slope of L_0. However, these three conditions cannot be satisfied simultaneously. Hence A splits S^2 into two halves. T cannot jump from one half into the other, except through the edge, where the boundaries are glued.

Together A and T split S^2 into several domains: $D_1, D_2, \ldots$. By construction, for a fixed i, the number of points in $C^{3\mathrm{PI}}(x) \cap \Pi(x, \alpha)$ is the same for all $\alpha \in D_i$. If D_i contains k IPs, it will be called a kIP domain. Table 2 lists how many IPs there are inside each D_i shown in Fig. 8.

Suppose now that interrupted illumination takes place. In a similar fashion, define several curves on the surface of S^2. The first three curves are obtained by considering unit vectors perpendicular to each of the three 3PI axes. They are denoted $A_k, k = 1, 2, 3$. The second set of

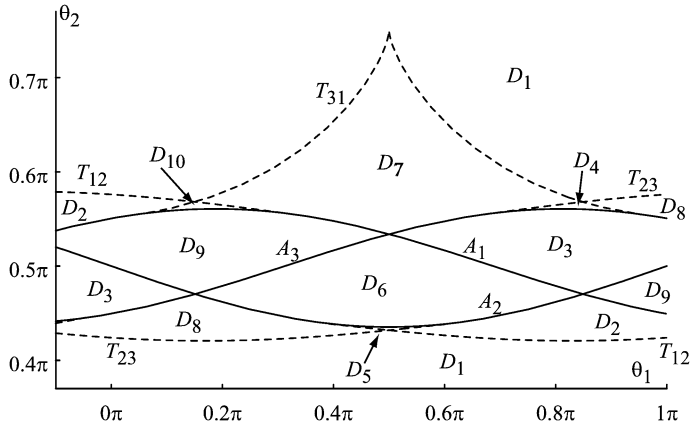

Fig. 9. The interrupted illumination case, $x = (-0.5, 0, 0)$.

Table 3
The interrupted illumination case. Distribution of intersection points over the subintervals of $I^{3\mathrm{PI}}(x)$, $x = (-0.5, 0, 0)$, for various domains

	D_1	D_2	D_3	D_4	D_5	D_6	D_7	D_8	D_9	D_{10}
(b_1, b_2)	0	2	0	0	2	1	0	0	1	2
(b_2, t_1)	1	1	2	3	1	1	3	1	2	3
(t_2, t_3)	0	0	1	2	2	1	0	2	0	0

curves is obtained by restricting s in (5.1) to the intervals $[b_1, b_2]$, $[b_3, t_1]$, and $[t_2, t_3]$. These curves are denoted T_{12}, T_{31}, and T_{23}, respectively. A typical situation for $x = (-0.5, 0, 0)$ is shown in Fig. 9 (see also Table 3).

It is clear that for all x near x_0 a similar diagram applies. By this we mean that one diagram can be smoothly deformed into the other, and in corresponding domains the number of IPs and their distribution over the subintervals in $I^{3\mathrm{PI}}$ stays the same. An essential change is possible only in a neighborhood of x where a "critical event" occurs: three boundaries intersect each other at one point on S^2. We now classify all possible critical events. Denote a point on a A curve by 1, an interior point of a T curve by 2, and a boundary point of a T curve by 3 (see Fig. 10). Thus, the following triple intersections are possible: 111, 112, 113, 122, 123, 133, 222, 223, 233, 333.

Clearly, cases 222, 223, 233, and 333 are not possible. Otherwise, they would mean that there exists a plane tangent to C at three points. From Lemmas 2–5, cases 111, 112, 122, are impossible, and case 133 implies that x belongs to the boundary between X_1 and X_3. Therefore, the remaining new cases are 113 and 123. It appears quite difficult to find analytically all x where these intersections occur. However, they can be found numerically.

If Case 113 occurs, there exist two 3PI lines such that the plane determined by the lines is tangent to C at one of their endpoints. Without loss of generality assume that this happens at $s = 0$. Consider $DP(0)$. By construction, $\hat{x} \in \Gamma_2 \cup \Gamma_{-2}$. Assume, for example, that $\hat{x} \in \Gamma_2$. By assumption, the projection of the other 3PI line onto $DP(0)$ is parallel to L_0. Let s_b and s_t denote the endpoints of that 3PI line. Since $\hat{x}$ is located between s_b and s_t and $2\pi < s_t - s_b < 4\pi$, we conclude $s_b \in \Gamma_1$ and $s_t \in \Gamma_3$. Cases $4\pi < s_t < s_3^{\mathrm{cr}}$ and $s_3^{\mathrm{cr}} < s_t < 6\pi$ are illustrated in Fig. 11, top panel. Recall that s_3^{cr} is the point where the line parallel to L_0 is tangent to Γ_3. Such a line

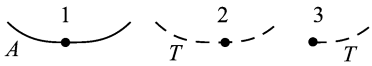

Fig. 10. Possible locations of a point $\alpha \in S^2$ on various curves.

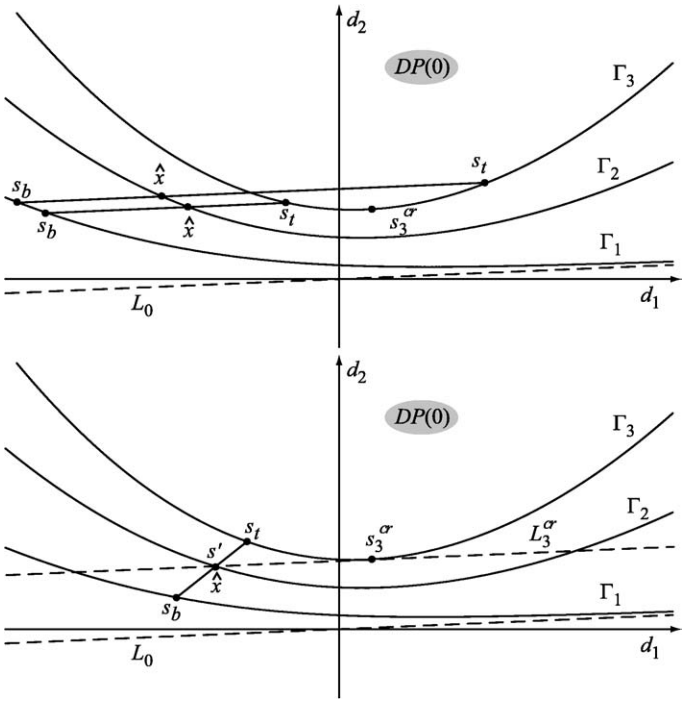

Fig. 11. Cases 113 (top panel) and 123 (bottom panel).

is denoted L_3^{cr} (see Fig. 2). Figure 11 suggests also a procedure for finding x where Case 113 occurs.

(1) Pick $s_t \in (4\pi, 6\pi)$ and determine the parameter value s' where the line segment with endpoints s_b, s_t and parallel to L_0 intersects Γ_2. By construction, $\hat{x}$ coincides with the point s' on Γ_2;
(2) Locate x, which is the point of intersection of the line segments with endpoints $y(s_b)$, $y(s_t)$ and $y(0)$, $y(s')$, respectively;
(3) Rotate x back to the plane $x_3 = 0$ (cf. Section 3).

The case $\hat{x} \in \Gamma_{-2}$ can be treated in a similar fashion.

If Case 123 occurs, the plane tangent to an endpoint of a 3PI line of x is tangent to $C^{3\mathrm{PI}}(x)$ at an interior point. If $s = 0$ is the endpoint where the tangency occurs, then, as before, $\hat{x} \in \Gamma_2 \cup \Gamma_{-2}$ on $DP(0)$. Assume, for example, that $\hat{x} \in \Gamma_2$. As follows from the assumptions, $\hat{x} \in \Gamma_2 \cap L_3^{\mathrm{cr}}$ and $s_3^{\mathrm{cr}} \in I^{3\mathrm{PI}}(x)$. Thus, there exists another 3PI line of x with endpoints s_b, s_t such that $s_t > s_3^{\mathrm{cr}}$ and $s_b \in \Gamma_1$ (see Fig. 11, bottom panel). This suggests a procedure for finding x where Case 123

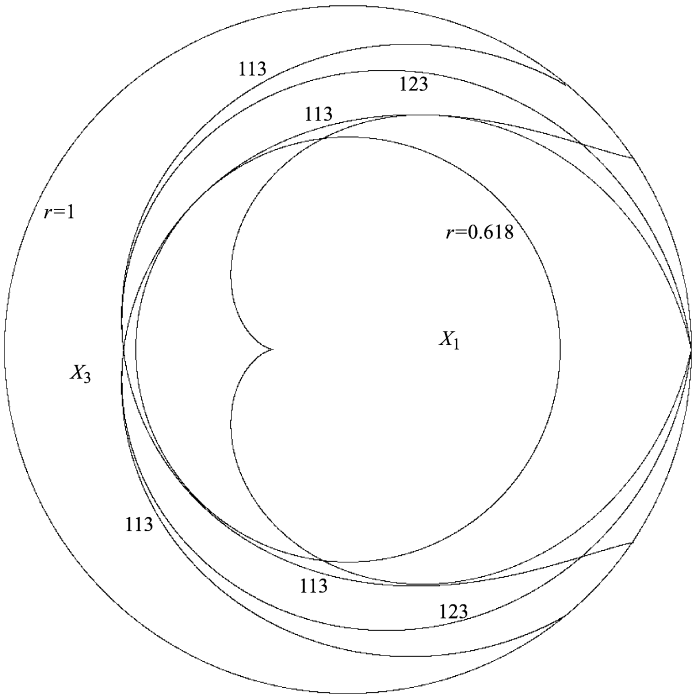

Fig. 12. Points where various critical events occur.

occurs. Let s' be the point on Γ_2 that corresponds to $\Gamma_2 \cap L_3^{\mathrm{cr}}$. s' should be to the left of s_3^{cr}, for otherwise $s_t > s_3^{\mathrm{cr}}$ implies $s_t - s_b > 4\pi$.

(1) Pick $s_t \in [s_3^{\mathrm{cr}}, s_t^{\max})$ and find the point where the line through $\hat{x}$ and s_t intersects Γ_1. Let s_b be the corresponding parameter value;
(2) Locate x, which is the point of intersection of the line segments with endpoints $y(s_b)$, $y(s_t)$ and $y(0)$, $y(s')$, respectively;
(3) Rotate x back to the plane $x_3 = 0$ (cf. Section 3).

Here $s_t^{\max}$ is found from the condition that the line through $s_t^{\max} \in \Gamma_3$ and $\hat{x}$ is vertical (i.e., if $s_t = s_t^{\max}$, then $s_t - s_b = 4\pi$). The case $\hat{x} \in \Gamma_{-2}$ can be treated in a similar fashion.

All the points found using the above two algorithms are shown in Fig. 12. The smallest distance from any of these points to the center of rotation is ≈ 0.618. If A and T were arbitrary curves, one could come up with other critical events. For example, a T curve could become tangent to an A curve at an interior point of T. In our case these events do not happen (cf. Lemmas 7 and 8). Thus, in situations of interest in medical applications ($r_{\mathrm{FOV}} \lesssim 0.5$), only the following two cases can happen: continuous illumination as shown in Fig. 8 (Table 2) and interrupted illumination as shown in Fig. 9 (Table 3).

6. Construction of the weight function *n*

Here we use the results of Sections 4 and 5 to construct n. Once n is known, we determine the filtering directions by locating the discontinuities of ϕ (cf. (2.7)).

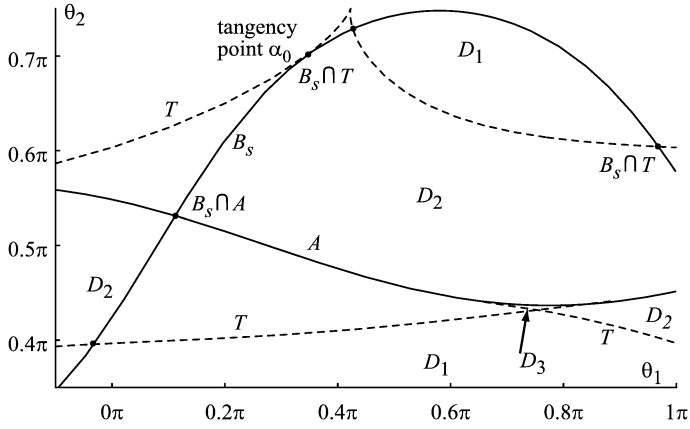

Fig. 13. Illustration of the curve B_s.

Fix $s \in I^{3\mathrm{PI}}(x)$ and consider the weight function $n(s, x, \alpha), \alpha \in \beta^{\perp}(s, x)$. Since n is normalized (cf. (2.6)), it might experience a jump when $\Pi(x, \alpha), \alpha \in \beta^{\perp}(s, x)$, is either tangent to $C^{3\mathrm{PI}}(x)$ or contains an endpoint of $C^{3\mathrm{PI}}(x)$ (i.e., contains a 3PI line of x). The jump of n across the direction when $\Pi(x, \alpha)$ is tangent to $C^{3\mathrm{PI}}(x)$ is not harmful to the FBP structure, because many other points will share the same tangent plane. However, the jump across a 3PI line might ruin the FBP structure, since 3PI lines depend on x. Thus, the condition on $n(s, x, \alpha)$ is that it should be continuous in $\alpha \in \beta^{\perp}(s, x)$ across all such jumps.

Similarly to what was done in Section 5, all directions $\alpha \in \beta^{\perp}(s, x)$ generate a curve on S^2, which is denoted B_s (see Fig. 13). Each intersection of B_s and A corresponds to a plane containing $L^{3\mathrm{PI}}(x)$. Each intersection of B_s and T corresponds to a plane tangent to $C^{3\mathrm{PI}}(x)$. At first, we will be interested primarily in intersections of B_s with A, because $n(s, x, \alpha)$ has to be continuous (in $\alpha \in \beta^{\perp}(s, x)$) across all of them.

Figures 8 and 9 suggest a procedure for assigning weights to IPs. For convenience of notation, in this section the points on the helix $y(s) \in C$ will be referred to by using only the corresponding parameter value s. Fix $\alpha \in S^2$. The plane $\Pi(x, \alpha)$ intersects $C^{3\mathrm{PI}}(x)$ at some points $s_1(\alpha, \alpha \cdot x), s_2(\alpha, \alpha \cdot x), \ldots$. Suppose $\alpha \in D_j$ for some j. By construction, the number of IPs and their distribution over $I^{3\mathrm{PI}}(x)$ remains the same for all other $\alpha \in D_j$. Thus, the weights that will be assigned to these IPs should remain the same for all $\alpha \in D_j$. Consequently, if the IPs are arranged in the ascending order $s_1 < s_2 < \cdots$, the weight assigned to an IP s_k depends only on k. The distribution of weights among IPs might change from one domain to another.

From Figs. 8 and 9 we see that the jumps across an A-curve can only be of the two types: from a 3IP domain to a 3IP domain and from a 3IP domain to a 5IP domain. These jumps will be called 3-to-3 and 3-to-5 jumps, respectively. This is in agreement with the discussion in Section 4. Fix $s \in I^{3\mathrm{PI}}(x)$ and find a point $\alpha_0 \in B_s \cap A$ where B_s has a 3-to-3 jump. Using the terminology of Section 4, Case II takes place. By construction, s is among the IPs on each side of A. If s is assigned different weights on different sides of A, then $n(s, x, \alpha)$ will have a discontinuity across $\alpha = \alpha_0$. To avoid the discontinuity the weight should be the same on both sides. The simplest way to achieve this is to assume that inside any 3IP domain each IP has weight $1/3$.

Consider now the case when B_s has a 3-to-5 jump across $\alpha_0 \in B_s \cap A$. Using the terminology of Section 4, Case I takes place. Again, the point s is obviously among the IPs on each side of A in a neighborhood of α_0. Consequently, s cannot be among a newly-born pair of points. Thus,

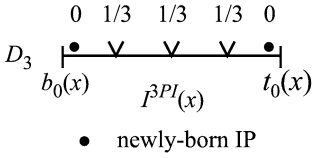

Fig. 14. Distribution of weights inside the 5IP domain in the case of continuous illumination (cf. Fig. 8).

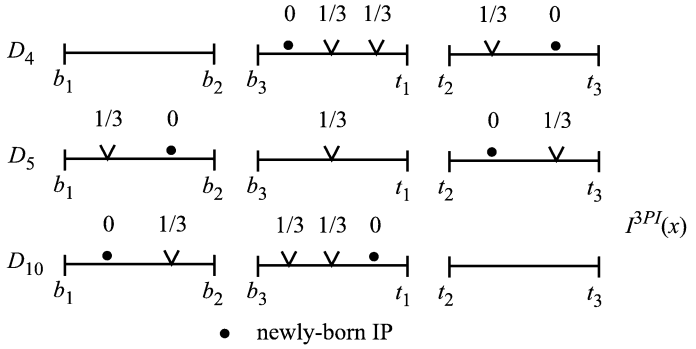

Fig. 15. Distribution of weights inside the 5IP domains in the case of interrupted illumination (cf. Fig. 9).

in order to avoid a discontinuity of $n(s, x, \alpha)$ across $\alpha = \alpha_0$, the newly-born points are assigned weights that add up to zero (e.g., zero each), and the remaining points are assigned weight $1/3$ each.

To summarize, our discussion leads to the following rule:

(1) In 1IP domains the only IP gets weight $n = 1$;
(2) In 3IP domains each IP gets weight $n = 1/3$;
(3) In 5IP domains each newly-born IP gets weight $n = 0$, and all the remaining IPs get weight $n = 1/3$.

Using the discussion in Section 4, Figs. 8 and 9, and Tables 2 and 3, the distribution of weights in the 5IP domains, which is obtained from this rule, is shown in Figs. 14 and 15.

As follows from (2.7)–(2.9), for each $s \in I^{3\mathrm{PI}}(x)$ the filtering directions are determined by finding the discontinuities of $\phi(s, x, \alpha) = \operatorname{sgn}(\alpha \cdot \dot{y}(s))n(s, x, \alpha)$.

6.1. *Discontinuities of* $\operatorname{sgn}(\alpha \cdot \dot{y}(s))$

The factor $\operatorname{sgn}(\alpha \cdot \dot{y}(s))$ is discontinuous when $\Pi(x, \alpha)$ is tangent to $C^{3\mathrm{PI}}(x)$ at $y(s)$. Suppose this happens when $\alpha = \alpha_0$. As is easily seen by considering $DP(s)$, a small rotation of $\Pi(x, \alpha)$ across $\alpha = \alpha_0$ does not change the number of IPs. More generally, their distribution over the subintervals of $I^{3\mathrm{PI}}(x)$ remains the same. What changes is the location of the IP s relative to other IPs. For example, if s is the kth IP, then it will become either $(k-1)$st or $(k+1)$st IP. The two points approach each other, collide, and then change places. On S^2 this shows up when B_s is tangent to a T curve (cf. assertion (b) of Lemma 6). Since the number of IPs remains the same in a neighborhood of α_0, B_s does not cross the T-curve, but stays on one side of it near α_0.

By construction, ϕ may have two different values of discontinuity across $\alpha = \alpha_0$. The first possibility occurs when s is an ordinary IP before and after the jump. We call it an O-to-O jump. Thus, $n(s, x, \alpha) = 1/3$ if $\alpha = \alpha_0^+$ and $\alpha = \alpha_0^-$, and the magnitude of the discontinuity of ϕ is 2/3. The second possibility occurs when s is an ordinary IP on one side of α_0 (with $n = 1/3$), and a newly-born IP - on the other side (with $n = 0$). We call it an O-to-NB jump. Now the magnitude of the discontinuity equals $1/3$.

Lemma 1. *A swap of two IPs involves a newly-born IP s if and only if B_s is tangent to a T-curve inside the 5IP domain of its birth.*

Proof. One direction is immediate. If the swap involves a newly-born IP, it must take place inside the 5IP domain where it is born, because this is the only domain where the IP is regarded as newly-born. To prove the opposite direction notice that any such swap involves two IPs located on an interval without any gap between them. Otherwise they will not be able to collide. Converting a 3D equation of a plane intersecting a helix into a 1D one, we immediately see that if two IPs collide at a point $s = s_0$, then s_0 is necessarily an extreme point among all IPs (i.e., either the smallest or the largest). Combining these two observations with Figs. 14 and 15 we finish the proof. □

Let us find the boundary on the detector between the two possible types of jump. Recall that s is fixed, but we now allow x to change slightly inside the 3PI window. Let $\alpha_0 = \alpha_0(x)$ denote the point where B_s is tangent to T (i.e., $\Pi(x, \alpha_0)$ is tangent to $C^{3\mathrm{PI}}(x)$ at s). As x changes, α_0 can move into a different domain only in one of the following cases (see Fig. 16):

(1) α_0 moves onto the A curve and disappears;
(2) the 5IP domain collapses into a point;
(3) α_0 moves through α_{cr}, where two T curves intersect.

In the first two cases $\alpha_0 \in A$ implies $\hat{x} \in \Gamma_{\pm 2}$. Recall that if two T curves do not intersect, then locally there is one-to-one correspondence between planes through x (and, hence, directions α) that are tangent to $C^{3\mathrm{PI}}(x)$ and the points of tangency. Considering the limit as $\alpha_0 \to A$, we conclude from the proof of assertion (c) of Lemma 6 that s is an endpoint of the $L^{3\mathrm{PI}}(x)$ axis that generated the curve A, so $\hat{x} \in \Gamma_{\pm 2}$. In the third case we conclude that $\Pi(x, \alpha)$ is tangent to $C^{3\mathrm{PI}}(x)$ at $y(s)$ and at another point. This gives the boundaries $L^{\mathrm{cr}}_{\pm 2}$, $L^{\mathrm{cr}}_{\pm 3}$.

Let us prove that in Case 3 above $\alpha_0 = \alpha_{\mathrm{cr}}$ implies $\hat{x} \notin L^{\mathrm{cr}}_{\pm 3}$. Consider L^{cr}_3 first. Let s^{cr}_3 be the point where L^{cr}_3 is tangent to Γ_3. It suffices to show that $s^{\mathrm{cr}}_3 \notin I^{3\mathrm{PI}}(x)$ whenever $\hat{x} \in L^{\mathrm{cr}}_3$

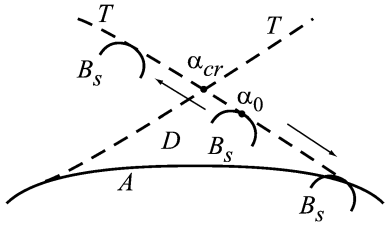

Fig. 16. Different possibilities for α_0 to change location.

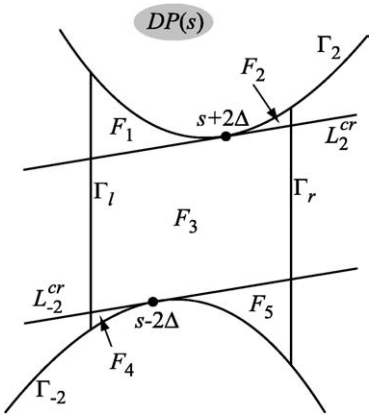

Fig. 17. Domains on the detector plane where the jumps of ϕ, which are caused by a discontinuity of the factor $\operatorname{sgn}(\alpha \cdot \dot{y}(s))$, remain the same.

and $x_1^2 + x_2^2 < 0.618^2$. Pick a point $x^a \in U$ such that $(x_1^a)^2 + (x_2^a)^2 < 0.618^2$ and $\hat{x}^a \in L_3^{\mathrm{cr}}$. We can verify numerically that $t_3(x^a) < s_3^{\mathrm{cr}}$, that is $s_3^{\mathrm{cr}} \notin I^{3\mathrm{PI}}(x^a)$. Suppose there exists x^b such that $(x_1^b)^2 + (x_2^b)^2 < 0.618^2$, $\hat{x}^b \in L_3^{\mathrm{cr}}$, and $t_3(x^b) > s_3^{\mathrm{cr}}$. Connect x^a and x^b by a continuous curve, whose projection belongs to L_3^{cr} and which is inside the cylinder $r = 0.618$. By continuity there must be a point x^c on the curve with $t_3(x^c) = s_3^{\mathrm{cr}}$. This implies that Case 123 takes place, so x^c must be outside the cylinder $r = 0.618$ (cf. Fig. 12). This contradiction proves the desired assertion. In a similar fashion we prove that $\hat{x} \notin L_{-3}^{\mathrm{cr}}$. Consequently, $L_{\pm 2}^{\mathrm{cr}}$ split the 3PI window into five domains $F_1, F_2, \ldots, F_5$ as shown in Fig. 17, and inside each domain the jump of ϕ, which arises because of a discontinuity of $\operatorname{sgn}(\alpha \cdot \dot{y}(s))$, is the same. Here Γ_l and Γ_r denote the boundary of the cylinder $x_1^2 + x_2^2 = 0.618^2$ projected onto the detector plane.

6.2. *Discontinuities of* $n(s, x, \alpha)$

By construction, n is continuous across all A curves. So a discontinuity of n can occur only when B_s intersects a T curve. Clearly, every time B_s crosses a T curve the number of IPs changes by two. Thus, there can be either 1-to-3 jumps or 3-to-5 jumps. In the former case, $n = 1$ in the 1IP domain, $n = 1/3$ in the 3IP domain, so the magnitude of the jump is $2/3$.

Next consider 3-to-5 jumps. Not all of them result in a discontinuity of n. Clearly, n is discontinuous only if s is regarded as a newly-born IP on the side of T where the 5IP domain D of its birth is located. In this case the magnitude of the jump is $1/3$. Let us assume that s has this property. The following statements can be made about the behavior of B_s inside D.

- B_s is tangent from the inside to a T boundary of the 5IP domain D (by Lemma 1);
- B_s cannot intersect A more than once, and B_s has no self-intersections;
- Intersection of B_s and T when B_s exits D is transversal (otherwise T will not actually exit D, cf assertion (c) of Lemma 6);
- B_s cannot be tangent to T at another point inside D (Recall that existence of a point of tangency implies a swap of two extreme IPs. If there are two swaps inside a 5IP domain D, then the IP s is either IP#1 or IP#2 and either IP#4 or IP#5, which is not possible);
- $\alpha_{\mathrm{cr}} \notin B_s$ for a generic $s \in I^{3\mathrm{PI}}(x)$ (by Lemma 9).

Let us discuss in more detail why Lemma 1 applies (cf. the first claim above). If s is a newly-born IP, by tracing B_s back to its intersection with A, we see that an IP must disappear. Clearly, s itself cannot disappear, because otherwise B_s terminates. Hence another IP must take its place as a newly-born IP. This means that a swap of s and another IP takes place inside the 5IP domain D, so Lemma 1 applies. Summarizing the above claims we conclude that in a neighborhood of D the curve B_s looks similar to the one shown in Fig. 18.

We have established also that conditions, which guarantee a 3-to-5 jump with a discontinuity of n, are exactly the same as those stated in Lemma 1. Consequently, the boundaries between the areas where this event takes and does not take place are the same as in Fig. 17.

Finally, we have to find the boundaries for the 1-to-3 jumps. First of all, such a jump can occur only if the projection of x onto $DP(s)$ is inside the 1PI window. Otherwise, no matter which plane through x and s is taken, there are at least two IPs: one is inside $I^{1\mathrm{PI}}(x)$, and the other one is s. Suppose a 1-to-3 jump takes place across $\alpha = \alpha_0$. Intersection of B_s and T at α_0 has to be transversal. If B_s is tangent to T at α_0, the number of IPs remains constant in a neighborhood of $\alpha = \alpha_0$ (cf. assertion (c) of Lemma 6). Again, s is fixed, and we allow x to change slightly inside the 1PI window. α_0 can cease to be a point of the 1-to-3 jump only in one of the following cases (see Fig. 19):

(1) α_0 moves through α_{cr} and becomes a 3-to-5 jump (Fig. 19, left panel);
(2) the 5IP domain D collapses into a point and α_0 moves onto A (Fig. 19, middle panel);
(3) α_0 becomes a point of nontransversal intersection of B_s and T, i.e. either T is nonsmooth at α_0 or B_s is tangent to T at α_0 (see Fig. 19, right panel).

In Case 1, $\hat{x} \in L^{\mathrm{cr}}_{-1,1}$ when $\alpha_0 = \alpha_{\mathrm{cr}}$ (see Lemma 10). Case 2 is essentially the same. In Case 3 we get L_0 and $\Gamma_{\pm 1}$ (see Lemma 11). Thus, the boundaries are $\Gamma_{\pm 1}$, $L^{\mathrm{cr}}_{-1,1}$, and L_0. The corresponding four domains $G_1, \ldots, G_4$ are shown in Fig. 20.

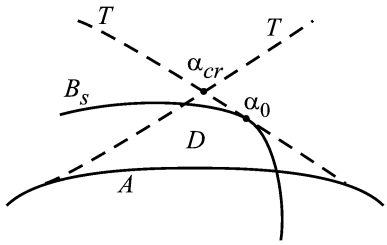

Fig. 18. A typical curve B_s when s is a newly-born IP inside the 5IP domain of its birth D.

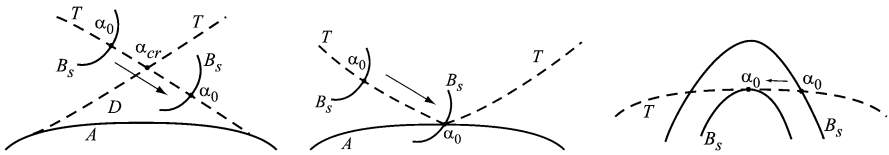

Fig. 19. Possible changes of a 1-to-3 jump.

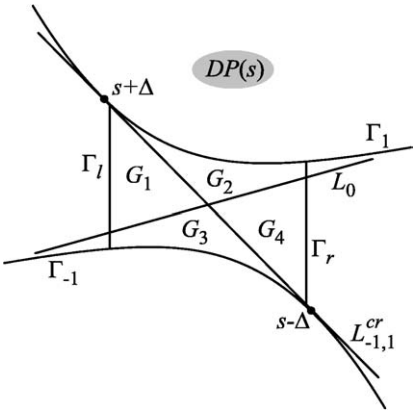

Fig. 20. Domains on the detector plane where the jumps of ϕ, which are caused by a discontinuity of the factor $n(s,x,\alpha)$, remain the same.

7. First reconstruction algorithm

Once the weight function n and filtering directions are found, the only remaining item that needs to be done is to determine the backprojection coefficients c_m (cf. (2.9)). The coefficients c_m are computed by analyzing the discontinuities of ϕ.

First consider the discontinuity of ϕ which arises because of the factor $\operatorname{sgn}(\alpha\cdot\dot{y}(s))$. In (2.8) this discontinuity will be assigned number $m=1$. Clearly, for any $x\in U$ and $s\in I^{3\mathrm{PI}}(x)$ the corresponding filtering line on $DP(s)$ passes through $\hat{x}$ and is parallel to $\dot{y}(s)$. The family of filtering lines parallel to $\dot{y}(s)$ is denoted $\mathcal{L}_0$ (see Fig. 21). As follows from the analysis in Section 6.1, given F_i all $x\in U$ with $\hat{x}\in F_i$ share the same type of jump (either O-to-O or O-to-NB) across the direction of the helical tangent. Picking at random one point from each of the domains and studying them numerically we conclude that O-to-O jumps occur when $\hat{x}\in F_3$, and O-to-NB jumps occur when $\hat{x}\in F_1\cup F_2\cup F_4\cup F_5$.

To find the corresponding backprojection coefficients c_1 we make the convention that filtering is always performed from left to right. Pick $x\in U$ so that $\hat{x}\in F_3$ (see Fig. 22). Following the convention, the corresponding vectors $\alpha^{\perp}(s,x,\theta_1)$, $\alpha_0:=\alpha(s,x,\theta_1)$, $\alpha_0^{\pm}:=\alpha(s,x,\theta_1\pm 0)$ are shown in Fig. 22. As follows from the discussion in Section 6, $n(s,x,\alpha_0)=1/3$. As is seen from the figure, $\operatorname{sgn}(\alpha_0^{\pm}\cdot\dot{y}(s))=\pm 1$. Thus, $\phi^{\pm}:=\phi(s,x,\theta_1^{\pm})=\pm 1/3$ and (2.9) implies $c_1(s,x)=2/3$, $\hat{x}\in F_3$.

Pick now $x\in U$ with $\hat{x}\in F_1$. Denote $L(\theta):=DP(s)\cap\Pi(x,\alpha(s,x,\theta))$. $L(\theta)$ is the projection of the plane through x with normal vector $\alpha(s,x,\theta)$. As θ increases, $\alpha(s,x,\theta)\in\beta^{\perp}(s,x)$ rotates in the clockwise direction on $DP(s)$. As follows from the discussion in Section 6, the following sequence of events takes place in a neighborhood of $\alpha=\alpha_0$ (see Figs. 23 and 24). First, $\Pi(x,\alpha(s,x,\theta))$ intersects $L^{3\mathrm{PI}}(x)$ and a pair of IPs is born. On the unit sphere this is seen as an intersection of curves B_s and A, after which B_s enters a 5IP domain D (see Fig. 24). Second, a swap of two IPs takes place. On $DP(s)$ this occurs when $\theta=\theta_1$, i.e. $\alpha_0\perp\dot{y}(s)$ ($L(\theta_1)=L_0'$ is parallel to the helical tangent). On S^2 this means that B_s is tangent to a T curve at $\alpha_0=\alpha(s,x,\theta_1)$. Finally, B_s exists the 5IP domain by intersecting a T curve. On $DP(s)$ this takes place when $L(\theta)$ is tangent to Γ_2 (i.e., $L(\theta)=L_1^{\tan}$). Thus, s is an ordinary IP before the swap, and is regarded as a

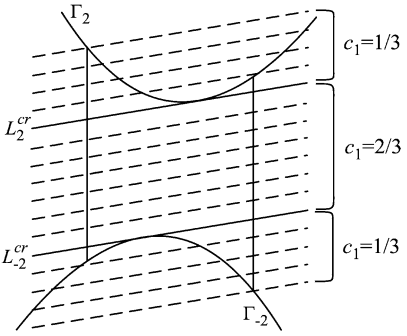

Fig. 21. Family $\mathcal{L}_0$ of filtering lines parallel to the helical tangent.

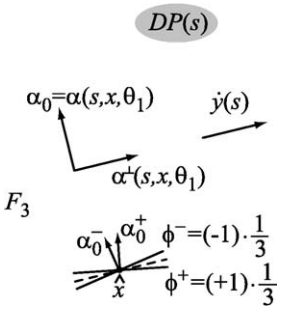

Fig. 22. Determination of c_1 in the case $\hat{x} \in F_3$. Middle part of $DP(s)$ is shown.

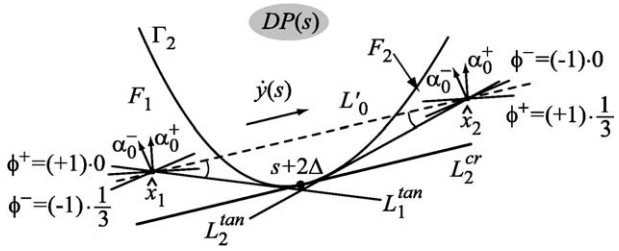

Fig. 23. Determination of c_1 in the cases $\hat{x} \in F_1$ and $\hat{x} \in F_2$. Top part of $DP(s)$ is shown.

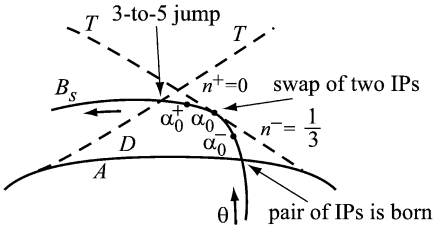

Fig. 24. Explanation of the case $\hat{x} \in F_1$.

newly-born IP after the swap. Consequently, $n^- := n(s,x,\alpha_0^-) = 1/3$ and $n^+ := n(s,x,\alpha_0^+) = 0$ (see Fig. 24). Also $\operatorname{sgn}(\alpha_0^\pm \cdot \dot{y}(s)) = \pm 1$ (see Fig. 23), so

$$c_1(s,x) = \phi^+ - \phi^- = (+1)0 - (-1)(1/3) = 1/3, \quad \hat{x} \in F_1. \tag{7.1}$$

In the case $\hat{x} \in F_2$ the situation is similar. The only difference is that the events unfold in reverse order. Thus, s is a newly-born IP before the swap, and a regular IP—after the swap. Since $\operatorname{sgn}(\alpha_0^\pm \cdot \dot{y}(s)) = \mp 1$, this gives $c_1(s,x) = 1/3$, $\hat{x} \in F_2$. The cases $\hat{x} \in F_4$ and $\hat{x} \in F_5$ can be analyzed in a similar fashion, and we get $c_1 = 1/3$, $\hat{x} \in F_4 \cup F_5$.

In summary, for any $\hat{x}$ there is only one line $L \in \mathcal{L}_0$ that contains $\hat{x}$. If $\hat{x} \in F_1 \cup F_2 \cup F_4 \cup F_5$, $c_1 = 1/3$. If $\hat{x} \in F_3$, $c_1 = 2/3$.

Next consider 1-to-3 jumps that occur because of the discontinuity of n. As follows from Fig. 19 and the discussion at the end of Section 6.2, the point α_0 where the jump takes place (= the point where B_s intersects T) depends smoothly on x provided that $\hat{x}$ stays inside each of the domains G_i, $i = 1,2,3,4$. Thus, we can pick a representative from each domain, determine what happens with it, and then extend the result by continuity to the entire domain. This gives the family of filtering lines tangent to $\Gamma_{\pm 1}$, which is denoted $\mathcal{L}_1$ (see Fig. 25). Now for each $\hat{x}$ within the 1PI window we take two lines from $\mathcal{L}_1$, i.e. for each $\hat{x} \in G_i$ there are two 1-to-3 jumps. Using the properties of the 1PI segment it is easy to see that one of the jumps occurs across a line tangent to $\Gamma_{\pm 1}$ at a point $s_t^{(1)} \in I^{1\mathrm{PI}}(x)$, and the other—across a line tangent to $\Gamma_{\pm 1}$ at a point $s_t^{(2)} \notin I^{1\mathrm{PI}}(x)$ (see Fig. 26). The former jump will be assigned number $m = 2$ in (2.8), and the latter—$m = 3$. Arguing as before (see Fig. 27), we get $c_2(s,x) = 2/3$, $c_3(s,x) = -2/3$, $\hat{x} \in G_i$, $i = 1,2,3,4$. These coefficients are illustrated in Fig. 26. Left panel illustrates the cases $\hat{x} \in G_2$ and $\hat{x} \in G_3$, and the right panel illustrates the cases $\hat{x} \in G_1$ and $\hat{x} \in G_4$.

Next consider 3-to-5 jumps that occur because of the discontinuity of n. As follows from Fig. 18 and the discussion in Section 6.2, the point where the jump takes place (= the point where B_s transversely intersects T, cf. Fig. 24) depends smoothly on x provided that $\hat{x}$ stays inside each of the domains F_i, $i = 1,\ldots,5$. Thus, we can pick a representative from each domain, determine what happens with it, and then extend the result by continuity to the entire domain. This gives that for any $\hat{x} \in F_1 \cup F_2 \cup F_4 \cup F_5$ only one such jump takes place, and the corresponding filtering line is tangent to $\Gamma_{\pm 2}$. In (2.8) this jump will be assigned number $m = 2$. By continuity we get

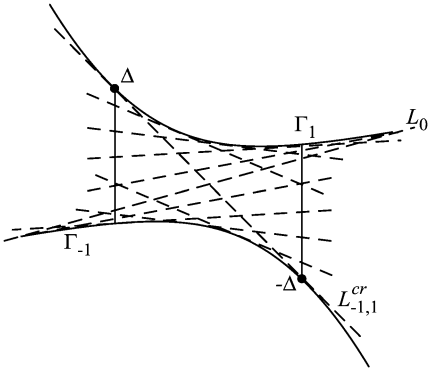

Fig. 25. Family $\mathcal{L}_1$ of filtering lines tangent to $\Gamma_{\pm 1}$.

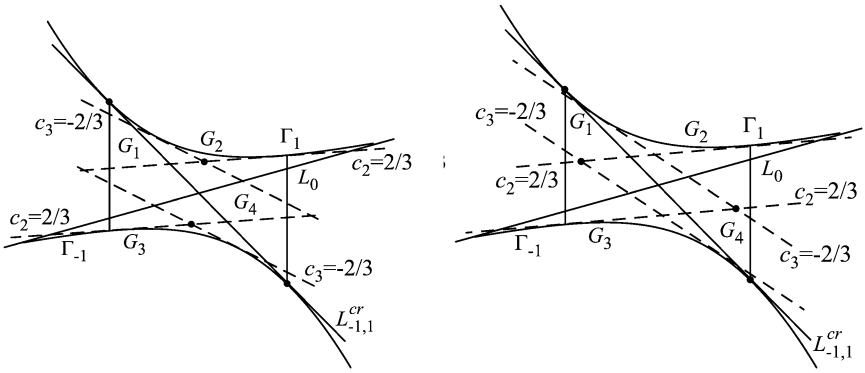

Fig. 26. How to choose filtering lines from $\mathcal{L}_1$ depending on the location of $\hat{x}$.

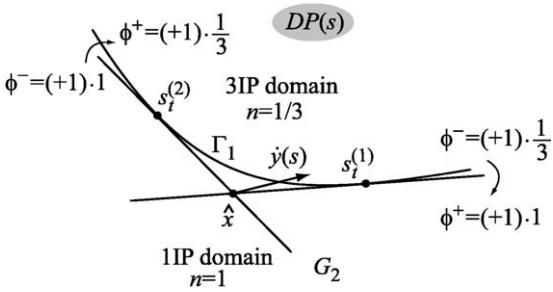

Fig. 27. Determination of c_2 and c_3 in the case $\hat{x} \in G_2$. Middle part of $DP(s)$ is shown.

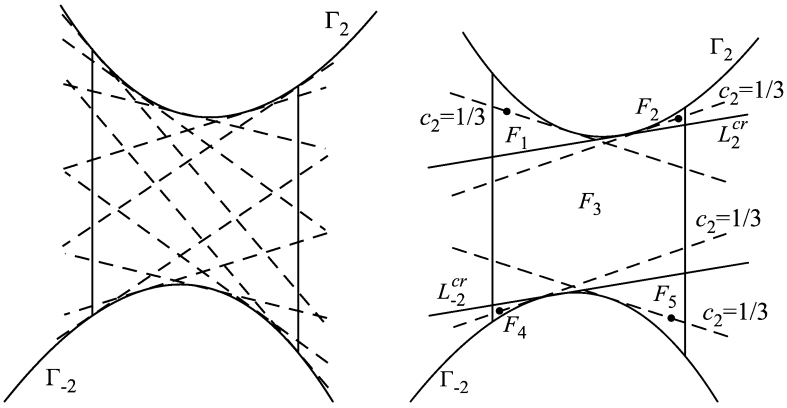

Fig. 28. Family $\mathcal{L}_2$ of filtering lines tangent to $\Gamma_{\pm 2}$.

the family of filtering lines tangent to $\Gamma_{\pm 2}$, which is denoted $\mathcal{L}_2$ (see Fig. 28, left panel). If $\hat{x} \in F_1 \cup F_4$, the point of tangency is to the right of $\hat{x}$. If $\hat{x} \in F_2 \cup F_5$, the point of tangency is to the left of $\hat{x}$ (see Fig. 28). Arguing as before with the help of Figs. 23 and 24 and the discussion around (7.1) we get in all cases $c_2 = 1/3$. When $\hat{x} \in F_3$ no 3-to-5 jump occurs.

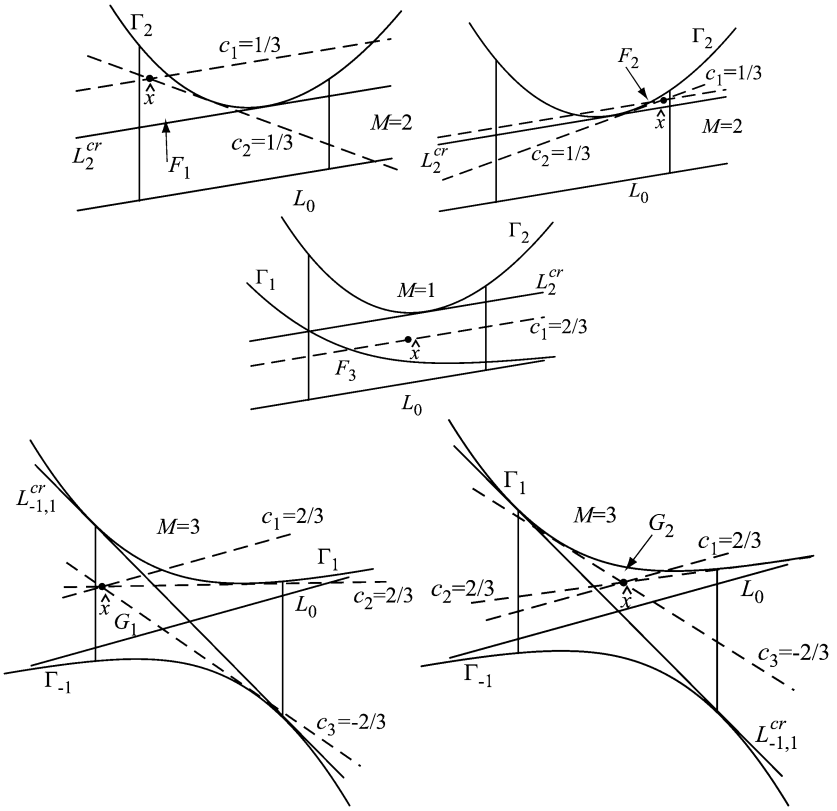

Fig. 29. Filtering lines and the associated constants c_m in different cases: $\hat{x} \in F_1$ (top left panel), $\hat{x} \in F_2$ (top right panel), $\hat{x} \in F_3$ and above Γ_1 (middle panel), $\hat{x} \in G_1$ (bottom left panel), $\hat{x} \in G_2$ (bottom right panel).

Figure 29 summarizes the information contained in Figs. 21–28. Assuming $\hat{x}$ is above L_0, Fig. 29 shows all possible cases where $\hat{x}$ might be and all the associated filtering directions and constants c_m. If $\hat{x}$ is below L_0, the situation is completely symmetric. Recall that in all cases the direction of filtering is assumed to be from left to right.

It follows from our construction (cf. Fig. 29) that $\theta_m(s,x)$ and $c_m(s,x)$ in the general reconstruction formula (2.8)–(2.9) depend on x only via $\beta(s,x)$. Therefore, we can replace x by $\beta(s,x)$ in the arguments of c_m and $\alpha^\perp$ and rewrite (2.8) in the form

$$f(x) = -\frac{1}{4\pi^2} \int\limits_{I^{3\mathrm{PI}}(x)} \frac{1}{|x - y(s)|} \sum_{m=1}^{M(s,\beta)} \Psi_m\big(s, \beta(s,x)\big)\, ds, \tag{7.2}$$

$$\Psi_m(s,\beta) := c_m(s,\beta) \int_0^{2\pi} \frac{\partial}{\partial q} D_f\big(y(q), \cos\gamma\beta + \sin\gamma\alpha^\perp(s,\beta,\theta_m)\big)\big|_{q=s} \frac{d\gamma}{\sin\gamma}. \tag{7.3}$$

Note also that given a filtering line L, all x whose projections belong to L and satisfy the rules mentioned above share the same filtering line L (cf. Fig. 29). Thus, (7.3) becomes a convolution, and the algorithm (7.2), (7.3) is of the convolution-based FBP type.

8. Improved reconstruction algorithm

Similarly to the 1PI algorithm proposed in [7], the 3PI algorithm developed in the preceding section is not optimal from the point of view of detector utilization and computational requirements. An improved 1PI algorithm was proposed in [8,10]. Analogously, an improved 3PI algorithm is proposed in this section. The new algorithm uses less detector data and requires fewer filtering lines.

Let $\psi(t)$ be any smooth function defined on $\mathbb{R}$ and with the properties $\psi(0) = 0$, $\psi'(t) > 0$, $t \in \mathbb{R}$. Define a new family of lines $\mathcal{L}_2'$ by requesting that any given line $L \in \mathcal{L}_2'$ has three points of intersection with $\Gamma_{\pm1} \cup \Gamma_{\pm2}$: s_1, s_2, s_3, and these points satisfy:

$$\begin{cases} s_1 - s = \psi(s_3 - s_2), & s + 2\pi < s_3 < s + 4\pi, \\ s_2 - s_3 = \psi(s - s_1), & s - 4\pi < s_3 < s - 2\pi. \end{cases} \tag{8.1}$$

The lines $L \in \mathcal{L}_2'$ can be parametrized, for example, by s_3, $2\pi < |s_3| < 4\pi$. Location of the IPs depends on where s_3 is and is illustrated in Fig. 30. Top half of the family $\mathcal{L}_2'$ that is obtained by choosing $\psi(t) = t$ in (8.1) is shown in Fig. 31.

Using the properties of ψ it is easy to establish that for each $\hat{x} \in F_1 \cup F_2 \cup F_4 \cup F_5$ there is a unique $L \in \mathcal{L}_2'$ that contains $\hat{x}$. Suppose, for example, $\hat{x} \in F_1$ (see Fig. 30, left panel). If there are two lines $L_2, L_2' \in \mathcal{L}_2'$ that contain $\hat{x}$, then there are two sets of values $\{s_1, s_2, s_3\}$ and $\{s_1', s_2', s_3'\}$ with $s_1' - s > s_1 - s$ and $s_3' - s_2' < s_3 - s_2$. However, the two conditions contradict (8.1). As is seen from Fig. 30, if $\hat{x} \to L_2^{\mathrm{cr}}$, then $s_2, s_3 \to s + 2\Delta$ and $s_1 \to s$. Similarly, if $\hat{x} \to L_{-2}^{\mathrm{cr}}$, then $s_2, s_3 \to s - 2\Delta$ and $s_1 \to s$.

More importantly, it turns out that in the case $\hat{x} \in F_1 \cup F_2 \cup F_4 \cup F_5$ it is possible to reduce the number of filtering directions from two to one. The additional benefit is improved detector usage. The discussion preceding Eq. (7.1) implies that s is a newly-born IP if and only if $\hat{x} \in F_1 \cup F_2 \cup F_4 \cup F_5$ and $L(\theta)$ belongs to one of the four wedges, which are labeled in Fig. 32 by I–IV. Hence, given x, α and s such that $y(s) \in \Pi(x, \alpha) \cap C$, by looking at $DP(s) \cap \Pi(x, \alpha)$ one can tell whether s is a newly-born IP or not. Going back to the weight function n, recall that the

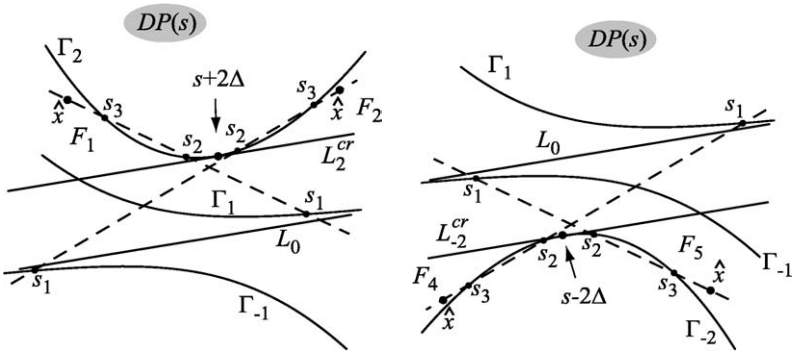

Fig. 30. Possible locations of the intersection points s_1, s_2, s_3.

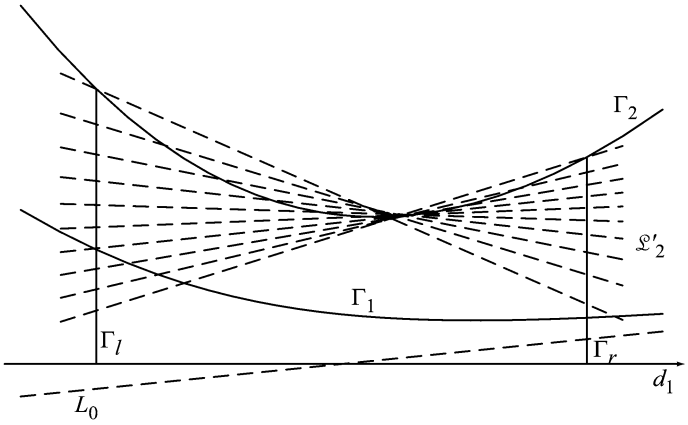

Fig. 31. Family of lines $\mathcal{L}'_2$, top half of the detector is shown.

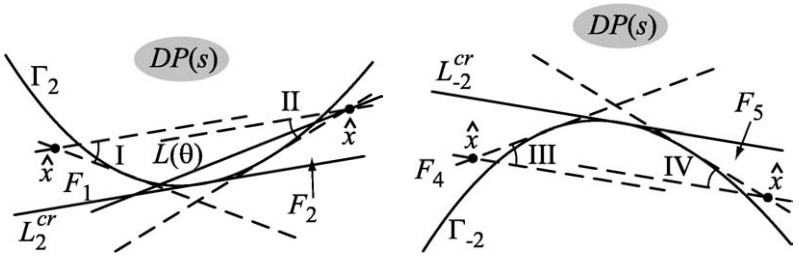

Fig. 32. Wedges I–IV where $L(\theta)$ has to be for s to be a newly-born IP. Left panel—top part of $DP(s)$, right panel—bottom part of $DP(s)$.

only requirement on weights assigned to newly-born IPs is that they add up to zero. We describe now a modified function n_{new}, that will result in an improved reconstruction algorithm. As usual, fix $x \in U$. Pick $s \in I^{3\text{PI}}(x)$ such that B_s passes through a 5IP domain D. Suppose $n_{\text{new}}(s, x, \alpha)$ is discontinuous in α at some point α_0 located on B_s between the points where B_s touches a T curve and where B_s exits D (see Fig. 33). This breaks B_s into five segments near D. Previously $n = 1/3$ if α belonged to segments 1,2, and 5, and $n = 0$ if α belonged to segments 3 and 4. Let $n_{\text{new}} = 1/3$ if α belongs to segments 1, 2, 4, and 5, and $n_{\text{new}} = -1/3$ if α belongs to segment 3. The first observation is that old and new n coincide outside 5IP domains. Secondly, newly-born IPs get weight either $1/3$ or $-1/3$. Finally, if we prove that given a pair of newly-born IPs their respective weights add up to zero, this will prove that the reconstruction algorithm based on n_{new} is theoretically exact.

To construct the required new jump, we postulate that it occurs when $L(\theta)$ (recall that θ parametrizes $\alpha(s, x, \theta) \in B_s$) coincides with $L_2 \in \mathcal{L}'_2$ for the chosen x and s. From the discussion at the beginning of this section, the jump is indeed located on the required segment of B_s. We now prove that the weights of the newly-born IPs add up to zero. Suppose $\hat{x} \in F_1$. By considering $L(\theta)$ on $DP(s)$ rotating in the counter clockwise direction just before it becomes parallel to $\dot{y}(s)$ we conclude that s is the smallest of the two IPs colliding. Since s is still regarded as a newly-born IP prior to the collision, we see that s is the first IP among all the IPs (see domain D_3 in Fig. 14 and domains D_4, D_{10} in Fig. 15). Considering three other cases and arguing in a similar

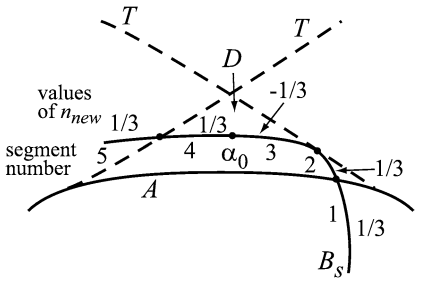

Fig. 33. Construction of n_{new}.

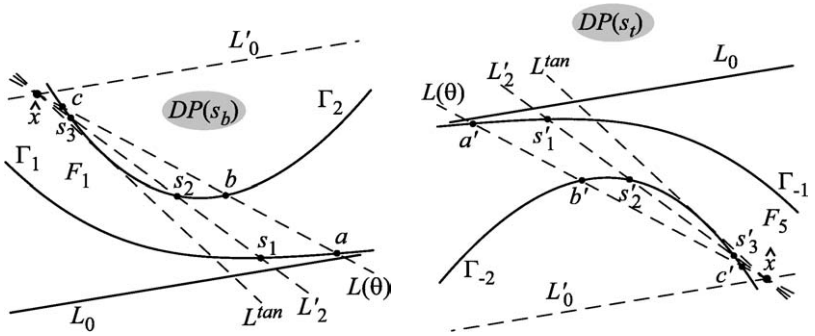

Fig. 34. Mutually incompatible locations of $L(\theta)$ on $DP(s_b)$ (left panel) and $DP(s_t)$ (right panel).

fashion we conclude that if $s_b < s_t$ is a pair of newly-born IPs, then either $\hat{x} \in F_1$ on $DP(s_b)$ and $\hat{x} \in F_5$ on $DP(s_t)$, or $\hat{x} \in F_2$ on $DP(s_b)$ and $\hat{x} \in F_4$ on $DP(s_t)$.

Suppose $\hat{x} \in F_1$. Comparing Figs. 33 and 34, left panel, implies that if $L(\theta)$ is between $L^{\tan}$ and L'_2, then $n_{\text{new}} = 1/3$; if $L(\theta)$ is between L'_0 and L'_2, then $n_{\text{new}} = -1/3$. The same holds when $\hat{x} \in F_5$. Thus, we have to show that if $L(\theta)$ is between L'_0 and L'_2 on $DP(s_b)$, then $L(\theta)$ is between $L^{\tan}$ and L'_2 on $DP(s_t)$. Alternatively, if $L(\theta)$ is between $L^{\tan}$ and L'_2 on $DP(s_b)$, then $L(\theta)$ is between L'_0 and L'_2 on $DP(s_t)$.

Let us study the first case. Let a, b, c and s_1, s_2, s_3 be the points of intersection of $L(\theta)$ and L'_2 with $\Gamma_1 \cup \Gamma_2$ on $DP(s_b)$, respectively (see Fig. 34, left panel). If $L(\theta)$ is above L'_2 on $DP(s_b)$:

$$s_3 - s_2 < c - b, \qquad a - s_b < s_1 - s_b. \tag{8.2}$$

Assume $L(\theta)$ is below L'_2 on $DP(s_t)$ to get a contradiction. The assumption implies:

$$s'_2 - s'_3 < b' - c', \qquad s_t - a' < s_t - s'_1, \tag{8.3}$$

where a', b', c' and s'_1, s'_2, s'_3 are points of intersection of $L(\theta)$ and L'_2 with $\Gamma_{-1} \cup \Gamma_{-2}$ on $DP(s_t)$, respectively (see Fig. 34, right panel).

Let $\Pi(x, \alpha), \alpha = \alpha(s, x, \theta)$, be the plane containing $L(\theta) \in DP(s_b)$ and $y(s_b)$. By construction, $\Pi(x, \alpha)$ coincides with the plane containing $L(\theta) \in DP(s_t)$ and $y(s_t)$. As is seen from Fig. 34, left panel, $b < c$ are the two highest IPs in $\Pi(x, \alpha) \cap C^{3\text{PI}}(x)$. Similarly, $c' < b'$ are the two lowest IPs in $\Pi(x, \alpha) \cap C^{3\text{PI}}(x)$. This conclusion also follows from the fact that by changing θ we can make the IPs b and c (as well as the IPs b' and c') collide, while only the extreme

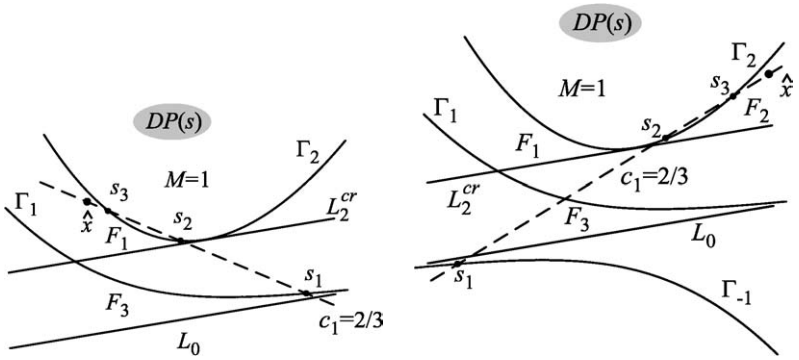

Fig. 35. Filtering lines and the associated coefficients c_m in different cases: $\hat{x} \in F_1$ (left panel), $\hat{x} \in F_2$ (right panel).

IPs can do that. Also, by construction, $s_b < a$ and $a' < s_t$ are the two lowest and highest IPs, respectively. Hence we can make the following identification:

$$s_t = c, \quad a' = b, \quad b' = a, \quad c' = s_b. \tag{8.4}$$

Using (8.2)–(8.4) gives

$$s_3 - s_2 < c - b = s_t - a' < s_t - s_1'. \tag{8.5}$$

From (8.1) and (8.2)–(8.4) we have

$$\psi(s_t - s_1') = s_2' - s_3' < b' - c' = a - s_b < s_1 - s_b = \psi(s_3 - s_2). \tag{8.6}$$

Since $\psi' > 0$, (8.5) and (8.6) contradict each other. The remaining cases when $L(\theta)$ is below L_2' and when $\hat{x} \in F_2 \cup F_4$ can be considered analogously.

Now it remains only to find the filtering directions and corresponding coefficients c_m. From Fig. 33 we see that n_{new} (and ϕ) is no longer discontinuous when B_s exits 5IP domains. Moreover, both $n_{\text{new}}(s, x, \alpha)$ and $\operatorname{sgn}(\alpha \cdot \dot{y}(s))$ change sign from one side of the point where B_s touches T to the other. Thus, ϕ is continuous there as well. The only actual discontinuity, which will be assigned $m = 1$, takes place when $L(\theta) = L_2'$. Using Fig. 33 and taking into account the sign of $\operatorname{sgn}(\alpha \cdot \dot{y}(s))$ we obtain that $\hat{x} \in F_1 \cup F_2 \cup F_4 \cup F_5$ implies $c_1 = 2/3$.

Thus, the top two panels shown in Fig. 29 should be replaced by the diagrams shown in Fig. 35. The case when $\hat{x}$ appears below L_0 (i.e., $\hat{x} \in F_4 \cup F_5$) can be obtained from Fig. 35 by symmetry with respect to the origin in the detector plane.

The form of the inversion formula (7.2), (7.3) remains the same. The first difference is that $M(s, \beta) = 1$ (instead of 2) when $\hat{x} \in F_1 \cup F_2 \cup F_4 \cup F_5$. The second difference is the direction of filtering, which is now determined using (8.1).

9. Numerical experiment

To test validity of the developed theory we wrote a code based on the improved reconstruction algorithm (7.2), (7.3) combined with the family $\mathcal{L}_2'$. The latter is based on $\psi(t) = t$ in (8.1). Simulation and reconstruction parameters are presented in Table 4. The clock phantom was used for simulations. The phantom is a superposition of a cylinder with radius 240 mm and two sets of

Table 4
Simulation and reconstruction parameters

Simulation parameters	
R (radius of the helix)	600 mm
h (pitch of the helix)	36 mm
Detector pixel size in each direction (as projected to isocenter)	10^{-3} rad $\times$ 0.6 mm
Number of detector rows	128
Number of detectors per row	950
Number of source positions per rotation	1000
Reconstruction parameters	
Number of points per convolution	2048
Voxel size in each direction	1.0 mm

balls. The first set consists of 12 balls with radius 24 mm, that are placed on a helix with radius 192 mm and pitch 28.8 mm. The second set consists of 12 balls with radius 12 mm, that are placed on a helix in the opposite direction with radius 120 mm and pitch 28.8 mm. The cylinder has density 1, and the balls have density 2.

The numerical implementation of the algorithm is done in native coordinates following [13]. The detector shape is cylindrical, so formula (46) in [13] is used to compute the derivative $\partial/\partial q$ in (7.3). Convolutions are computed using FFT with half-pixel shift as in [13]. Fourier transform of the kernel $1/\sin\gamma$ is computed analytically and truncated at the Nyquist frequency. Reconstruction results are shown in Fig. 36. The figure demonstrates the horizontal slice through the reconstructed image at $x_3 = 0.0$ on a 512×512 grid. We used the gray scale window [0.95, 1.05] to make low-contrast features visible.

As was mentioned before, the algorithms proposed here are of the most efficient FBP type (i.e., convolution-based with one-parametric families of filtering lines). Clearly, they are slower than the 1PI-based algorithms of [8,22], because more filtering lines are used. This can be viewed as the price one has to pay for using a significant amount of redundant data. On the other hand, the improved algorithm in Section 8 is essentially of the same efficiency as the approximate one proposed in [4]. The only difference between the two is how the family $\mathcal{L}_2'$ is defined. In [4] the lines in $\mathcal{L}_2'$ are tangent to $\Gamma_{\pm 2}$.

10. Auxiliary lemmas

Lemma 2. *Case* 111 *is not possible.*

Proof. If case 111 takes place, there exists a plane Π containing all three 3PI lines for x. Pick a point s_0 where this plane intersects $C^{1\mathrm{PI}}(x)$. Let $L := DP(s_0) \cap \Pi$. Since $I^{1\mathrm{PI}} \subset (b_3, t_1)$, points b_1, b_2, b_3 are below L_0, while their counterparts are above L_0. Equivalently, $b_i < s_0 < t_i$, $i = 1, 2, 3$. Clearly, none of the points b_1, b_2, b_3 can be on Γ_{-3} or below, and none of the points t_1, t_2, t_3 can be on Γ_3 or above. Otherwise, $t_i - b_i > 4\pi$ for at least one i. By assumption, L intersects $\Gamma_1 \cup \Gamma_2$ and $\Gamma_{-1} \cup \Gamma_{-2}$ at least at three points each. This implies that $L \cap \Gamma_2 \neq \emptyset$ and $L \cap \Gamma_{-2} \neq \emptyset$. Consequently, the only two possibilities for the location of L are illustrated in Fig. 37. Consider case A. The location of b_3, t_3 that minimizes $t_3 - b_3$ is shown in the figure. As is easily seen, $t_3 - b_3 > 4\pi$. In case B, there are only three points of intersection on each side of L_0. Therefore, the only possible location of b_1, b_2, b_3 and t_1, t_2, t_3, which is consistent with (3.25) is shown in Fig. 37. Since $b_2 \in \Gamma_{-2}$ and $t_2 \in \Gamma_2$, $t_2 - b_2 > 4\pi$. □

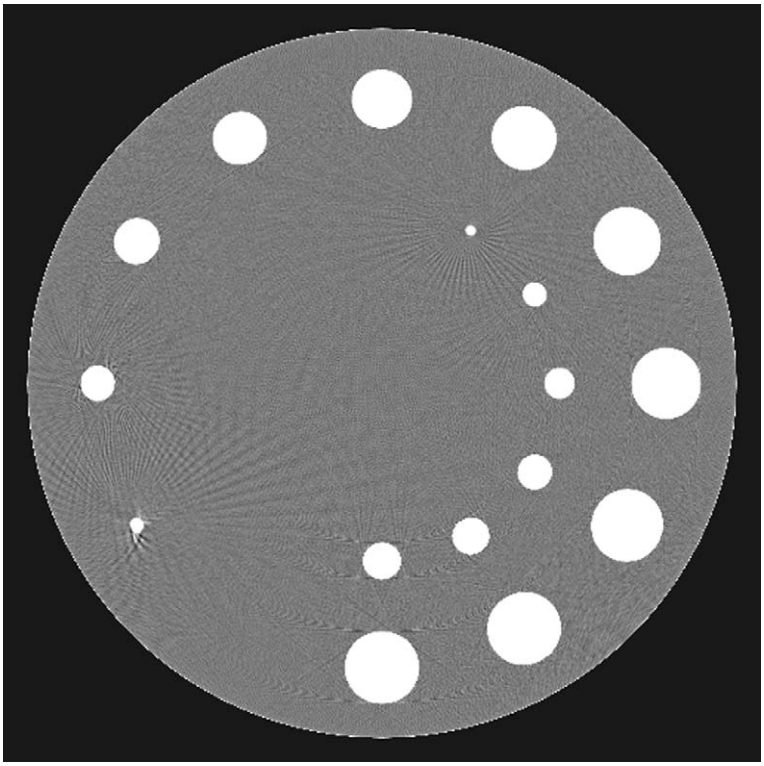

Fig. 36. Reconstruction results for the clock phantom.

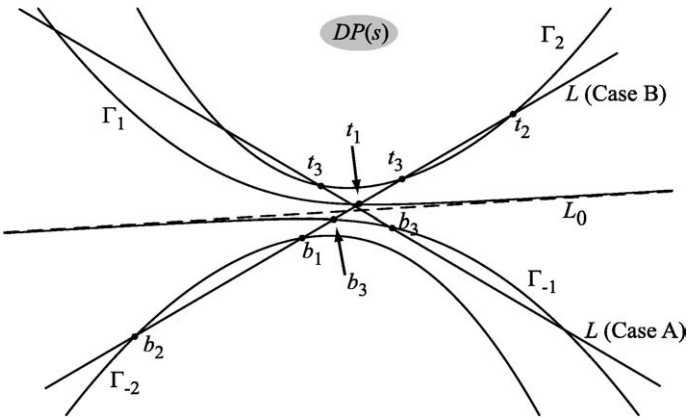

Fig. 37. Possible locations of line L if triple intersection 111 occurs.

Lemma 3. *Case* 112 *is not possible.*

Proof. If case 112 takes place, there exists a plane Π containing two 3PI lines for x and which is tangent to $C^{3\mathrm{PI}}(x)$ at an interior point s_t. Pick a point s_0 where this plane intersects $C^{1\mathrm{PI}}(x)$ and

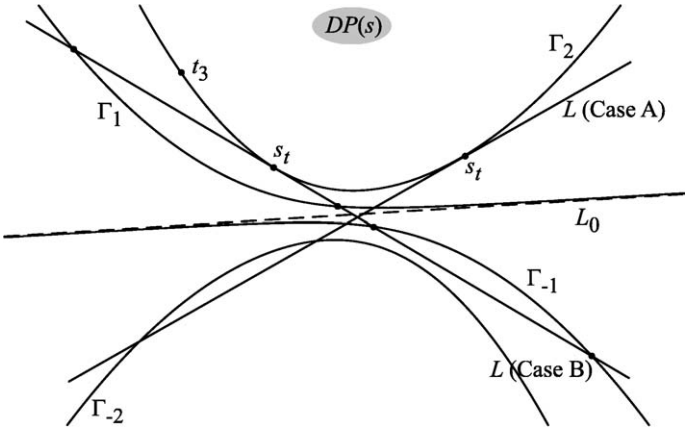

Fig. 38. Possible locations of line L if triple intersection 112 occurs.

denote $L = \Pi \cap DP(s_0)$. As before, $b_i \in \Gamma_{-1} \cup \Gamma_{-2}$, $t_i \in \Gamma_1 \cup \Gamma_2$, $i = 1, 2, 3$. Since $s_t \in I^{3\text{PI}}(x)$, s_t cannot be on Γ_{-3} (or below) and Γ_3 (or above). Since Π contains two 3PI lines, it must intersect $\Gamma_1 \cup \Gamma_2$ and $\Gamma_{-1} \cup \Gamma_{-2}$ at least at two points each. Consequently, s_t cannot be located on Γ_1 and Γ_{-1}. Because of the symmetry, we can assume without loss of generality that s_t is above L_0. The two possible cases are labeled A and B on Fig. 38. Case A is not possible, because there is only one point of intersection of Π with C above L_0 in addition to s_t (recall that s_t is an interior point of $I^{3\text{PI}}(x)$). Consider Case B. $s_t \in I^{3\text{PI}}(x)$ implies $s_t < t_3$, so Π contains $L_1^{3\text{PI}}(x)$ and $L_2^{3\text{PI}}(x)$. Pick any location where $t_3 \in \Gamma_2, t_3 > s_t$, might possibly be. To find the location of b_3 draw a straight line through t_3 and $\hat{x}$ and find where the line intersects $\Gamma_{-1} \cup \Gamma_{-2}$. It is clear that we necessarily get the contradiction $t_3 - b_3 > 4\pi$. □

Lemma 4. *Case* 122 *is not possible.*

Proof. If case 122 takes place, there exists a plane Π containing a 3PI line for x and tangent to $C^{3\text{PI}}(x)$ at two interior points $s_t^{(1)}, s_t^{(2)}$. Make the projection from $y(s_0)$, where $y(s_0) \in C^{1\text{PI}}(x) \cap \Pi$. As before, the points of tangency can only be located on $\Gamma_{\pm 1}$, $\Gamma_{\pm 2}$. They cannot be located on $\Gamma_{\pm 1}$, because in this case there will be an insufficient number of intersection points. The only two remaining cases are shown in Fig. 39 and labeled A and B. As before, Case A does not occur because it is not possible to find $t_3 > s_t^{(2)}$, so that $t_3 - b_3 < 4\pi$. Consider Case B. Since Π contains a 3PI line, the two intersection points s_1, s_2 shown in Fig. 39 are necessarily the bottom and top of a 3PI line of x. Since $s_2 - s_1 < 2\pi$, we get a contradiction. □

Lemma 5. *If Case* 133 *takes place for some x, then x belongs to the boundary between X_1 and X_3.*

Proof. If case 133 takes place, there exists a plane Π containing a 3PI line $L_i^{3\text{PI}}(x)$ of some x and tangent to $C^{3\text{PI}}(x)$ at the endpoints of $L_i^{3\text{PI}}(x)$: b_i, t_i. Make the projection from $y(s_0)$, where $y(s_0) \in C^{1\text{PI}}(x) \cap \Pi$. Let $L := DP(s_0) \cap \Pi$. As before, the points of tangency can only be located on $\Gamma_{\pm 1}$, $\Gamma_{\pm 2}$. Since the points of tangency coincide with the endpoints of $L_i^{3\text{PI}}(x)$, the only line that would satisfy $t_i - b_i < 4\pi$ is as shown in Fig. 40. This implies $t_i - b_i = 2\Delta$. Using the comment following (3.11), we finish the proof. □

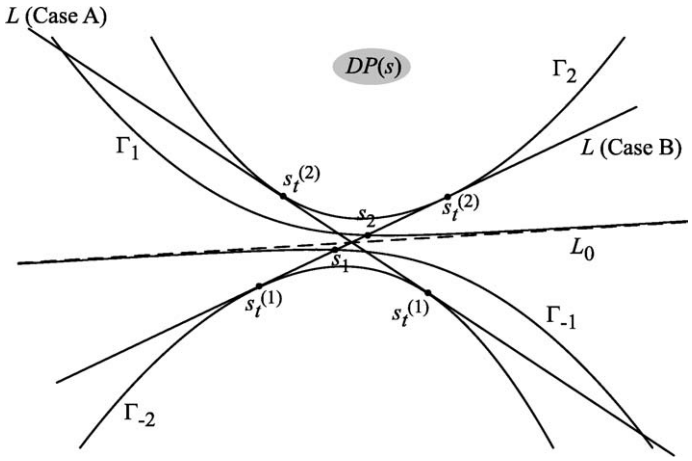

Fig. 39. Possible locations of line L if triple intersection 122 occurs.

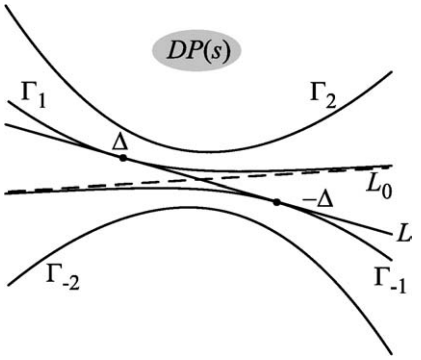

Fig. 40. The only possible location of line L if triple intersection 133 occurs.

Recall that for each $x \in U$ there exists the unique $\check{s}(x) \in I^{1\mathrm{PI}}(x)$ such that the plane $\check{\Pi}(x)$ through $y(\check{s}(x))$ and parallel to $\dot{y}(\check{s}(x))$, $\ddot{y}(\check{s}(x))$ contains x. This plane intersects C at only one point $y(\check{s}(x))$.

Lemma 6. (a) *A T curve is smooth everywhere, except possibly at a point $\alpha(\check{s}) \in T$;*
(b) *If $s \in I^{3\mathrm{PI}}(x)$ and $s \neq \check{s}(x)$, then B_s is tangent to T at the point $\alpha(s)$;*
(c) *If B_s is tangent to T at a point α_0 where T is smooth, then either $\alpha_0 = \alpha(s)$ or s is an endpoint of a PI segment* (1PI or 3PI) *containing x. In any case, the number of IPs in $\Pi(x, \alpha) \cap C^{3\mathrm{PI}}(x)$ remains the same for all $\alpha \in B_s$ in a neighborhood of α_0.*

Proof. (a) Since $|\alpha(s)| \equiv 1$, $\dot{\alpha}(s) \cdot \alpha(s) = 0$. It follows easily from (5.1) that $\dot{\alpha}(s) \cdot (x - y(s)) = 0$. Hence $\dot{\alpha}(s)$ is parallel to $(x - y(s)) \times \alpha(s)$. Thus, $\dot{\alpha}(s) = 0$ if and only if $\dot{\alpha}(s) \cdot [(x - y(s)) \times \alpha(s)] = 0$. From (5.1) we get that this condition is equivalent to

$$\big[\big(x - y(s)\big) \times \ddot{y}(s)\big] \cdot \big[\big(x - y(s)\big) \times \alpha(s)\big] = 0. \tag{10.1}$$

Since $\alpha(s) \perp (x - y(s))$, substitution of (5.1) into (10.1) proves the first assertion:

$$\big(x - y(s)\big) \cdot \big[\dot{y}(s) \times \ddot{y}(s)\big] = 0. \tag{10.2}$$

As is well known, (10.2) holds only if $s = \check{s}(x)$.

(b) Let θ be the polar angle parameterizing the great circle $(x - y(s))^{\perp}$. Then the curve B_s consists of the unit vectors $\alpha_1(\theta) \in (x - y(s))^{\perp}$. Obviously, $\dot{\alpha}_1(\theta) \perp \alpha_1(\theta)$ and $\dot{\alpha}_1(\theta) \perp (x - y(s))$. As we have already established, $\dot{\alpha}(s) \perp \alpha(s)$, $\dot{\alpha}(s) \perp x - y(s)$. If θ_0 is such that $\alpha_1(\theta_0) = \alpha(s)$, then $\dot{\alpha}_1(\theta_0)$ is parallel to $\dot{\alpha}(s)$.

(c) Suppose now B_s is tangent to T at some $\alpha_0 = \alpha(s_1)$, $s_1 \in I^{3\mathrm{PI}}(x)$. By the preceding argument $x - y(s)$ and $x - y(s_1)$ are parallel. If $s \neq s_1$, this implies that $y(s)$, $y(s_1)$ are endpoints of a PI line containing x. In any case, $B_s = B_{s_1}$, and the final assertion follows from the observation in the first paragraph of Section 6.1. □

Lemma 7. *A T curve cannot be tangent to an A curve at an interior point of T.*

Proof. Suppose T is tangent to A at a point $\alpha(s)$. If $s = \check{s}(x)$, $\Pi(x, \alpha(\check{s}))$ intersects the helix at only one point. However, $\Pi(x, \alpha(\check{s}))$ is supposed to also contain a 3PI line of x. Thus, $s \neq \check{s}(x)$ and T is smooth in a neighborhood of $\alpha(s)$. From assertion (b) of Lemma 6, B_s also is tangent to A at $\alpha(s)$. Considering vectors tangent to B_s and A at $\alpha(s)$ we conclude that $x - y(s)$ and the 3PI line corresponding to A are parallel. Thus, s is an endpoint of the 3PI line. Consequently, $\alpha(s)$ is an endpoint of a T curve. This contradicts the assumption that the point of tangency is an interior point of T. □

Lemma 8. *Two T curves cannot be tangent to each other, except when Case* 133 *takes place. In the latter case x belongs to the boundary between X_1 and X_3.*

Proof. Let α_0 be the point of tangency. If one of the curves is nonsmooth at α_0, then $\Pi(x, \alpha_0)$ intersects C at only one point (cf. Lemma 7). Thus, no second T curve can contain α_0. Therefore we can assume that both T curves are smooth at α_0. Let s_1 and s_2, $s_1 \neq s_2$, be values of the parameter such that $\alpha(s_1) = \alpha(s_2) = \alpha_0$. Arguing as in the proof of Lemma 7 we conclude that $x - y(s_1)$ and $x - y(s_2)$ are parallel. By construction, $\alpha_0 \perp \dot{y}(s_1)$ and $\alpha_0 \perp \dot{y}(s_2)$. These conditions imply

$$\begin{vmatrix} \cos s_1 - \cos s_2 & \sin s_1 - \sin s_2 & s_1 - s_2 \\ -\sin s_1 & \cos s_1 & 1 \\ -\sin s_2 & \cos s_2 & 1 \end{vmatrix} = 0. \tag{10.3}$$

Evaluating the determinant we get the familiar equation (cf. (3.9)):

$$\tan\big((s_2 - s_1)/2\big) = \frac{s_2 - s_1}{2}. \tag{10.4}$$

We have already determined that the line through $y(s_1)$, $y(s_2)$, contains x. Therefore, s_1 and s_2 are the endpoints of either a 1PI or 3PI segment of x. Since no solution to (10.4) exists that would satisfy $0 < |s_2 - s_1| < 2\pi$, s_1 and s_2 determine a 3PI segment of x and $s_2 - s_1 = 2\Delta$.

Summarizing, $\Pi(x, \alpha_0)$ contains a 3PI segment of x with the endpoints $y(s_1)$, $y(s_2)$, $s_2 - s_1 = 2\Delta$, and $\alpha_0 \perp \dot{y}(s_1)$, $\alpha_0 \perp \dot{y}(s_2)$. This implies that Case 133 takes place, so by Lemma 5 x belongs to the boundary between X_1 and X_3. □

Lemma 9. *Fix $x \in U$. There exist at most finitely many $s \in I^{3\mathrm{PI}}(x)$ such that $\alpha_{\mathrm{cr}} \in B_s$.*

Proof. Let $s_1, s_2 \in I^{3\mathrm{PI}}(x)$, $s_1 < s_2$, be two points with $\alpha(s_1) = \alpha(s_2) = \alpha_{\mathrm{cr}}$. From (10.4) in the proof of Lemma 8 and (3.9) $s_2 = s_1 + 2\Delta$. Thus, there is at most finitely many planes $\Pi(x, \alpha_{\mathrm{cr}})$ that contain x and are tangent to C at two points. If $\alpha_{\mathrm{cr}} \in B_s$, then s belongs to $\Pi(x, \alpha_{\mathrm{cr}}) \cap C^{3\mathrm{PI}}(x)$ and the desired assertion follows. □

Lemma 10. *Let α_{cr} be a point where two T curves intersect. Suppose Case* 1 *of Section* 6.2 *happens (cf. Fig.* 19*, left panel). Suppose $\alpha_0 = \alpha_{\mathrm{cr}}$ for some $x \in U$ and $\hat{x}$ is inside the 1PI window. Then $\hat{x} \in L^{\mathrm{cr}}_{-1,1}$.*

Proof. By construction $\hat{x}$ belongs to a double tangent line and $s \in I^{1\mathrm{PI}}(x)$. As before, $t_i \in \Gamma_1 \cup \Gamma_2$, $b_i \in \Gamma_{-1} \cup \Gamma_{-2}$, and the points of tangency are confined to $\Gamma_{\pm 1} \cup \Gamma_{\pm 2}$. The possible double tangent lines subject to this constraint and different from $L^{\mathrm{cr}}_{-1,1}$ are shown in Fig. 41 (see top and bottom left panels).

Consider Case A (see Fig. 41, top panel). Since $s_t \in I^{3\mathrm{PI}}(x)$, $t_i > s_t$ for $i = 0$ if $x \in X_1$ or some $i \in \{1, 2, 3\}$ if $x \in X_3$. Since $\hat{L}_i^{3\mathrm{PI}}(x)$ contains $\hat{x}$ and $b_i \in \Gamma_{-1} \cup \Gamma_{-2}$, we immediately get the contradiction $t_i - b_i > 4\pi$. Recall that $\hat{L}_i^{3\mathrm{PI}}(x)$ denotes the projection of $L_i^{3\mathrm{PI}}(x)$ onto $DP(s)$. Cases B and C can be ruled out in a similar fashion.

Consider Case D (see Fig. 41, bottom panels). As is seen from Figs. 8 and 9, α_{cr} always belongs to the boundary of a 1IP domain. In particular, in any neighborhood of $(x, \alpha_{\mathrm{cr}})$ there is always a pair (x', α'), $\alpha' \in B_s$, such that $\Pi(x', \alpha')$ has only one IP with $C^{3\mathrm{PI}}(x')$ (cf. Figure 19, left panel). Since $s_t^{(2)} - s_t^{(1)} > 4\pi$, we have $x \notin X_1$. Therefore, $x \in X_3$. By construction, $t_3 > s_t^{(2)}$. This implies that b_3 is to the right of the point where L intersects Γ_{-1} (see Fig. 41, bottom right

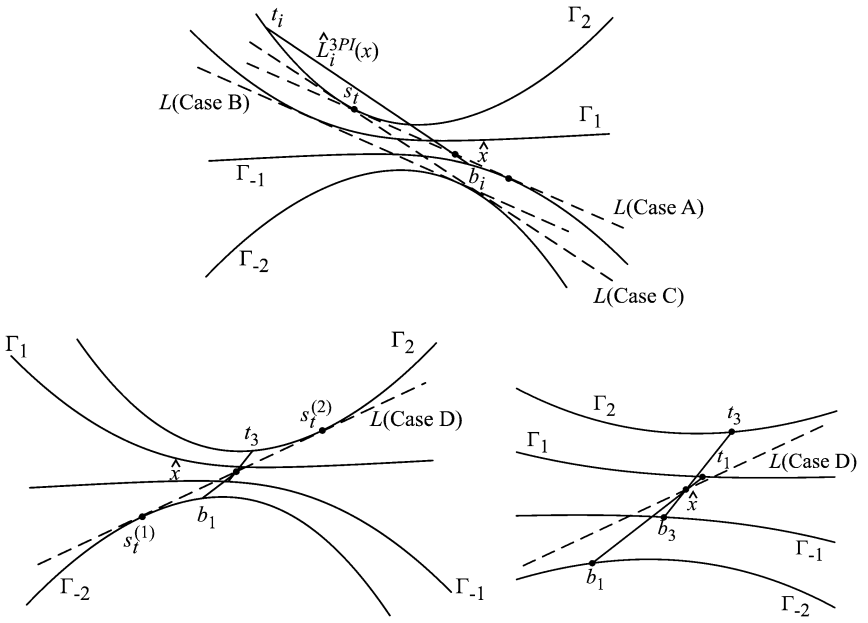

Fig. 41. Various possible double tangent lines $L = DP(s) \cap \Pi(x, \alpha_{\mathrm{cr}})$.

panel). In a similar fashion, $b_1 < s_t^{(1)}$. This implies that t_1 is to the left of the point where L intersects Γ_1. Consequently, for any (x', α'), $\alpha' \in B_s$, sufficiently close to $(x, \alpha_{\rm cr})$, $\Pi(x, \alpha) \cap C^{\rm 3PI}(x)$ contains at least three points (which are inside (b_3, t_1)). This contradiction rules out Case D. □

Lemma 11. *Under the assumptions of Case* 3 *in Section* 6.2*, let* $x = x_{\rm cr}$ *when* α_0 *becomes a point of nontransversal intersection of* B_s *and* T*. Then* $\hat{x}_{\rm cr} \in L_0 \cup \Gamma_{\pm 1}$.

Proof. If T is not smooth at α_0, assertion (a) of Lemma 6 implies $\hat{x}_{\rm cr} \in L_0$. Suppose now $\hat{x}_{\rm cr} \notin L_0$ and B_s is tangent to T at α_0. By assertion (c) of Lemma 6, either $\Pi(x_{\rm cr}, \alpha_0)$ contains $\dot{y}(s)$ or $\hat{x}_{\rm cr} \in \Gamma_{\pm 1}$ (recall that $\hat{x}_{\rm cr}$ is inside the 1PI window). Suppose $\Pi(x_{\rm cr}, \alpha_0)$ is tangent to C at $y(s)$. As follows from the observation in the first paragraph of Section 6.1, B_s stays on one side of T in a neighborhood of α_0. By the assumptions in Case 3 (see Fig. 19, right panel), there exist two distinct points $s_1(x), s_2(x) \in I^{\rm 3PI}(x)$ such that $s_1 - s_2 \to 0$ and $\alpha(s_1), \alpha(s_2) \to \alpha_0$ when $x \to x_{\rm cr}$. But this is not possible because of the properties of the curves Γ_j. This leaves the only alternative $\hat{x}_{\rm cr} \in \Gamma_{\pm 1}$. □

References

[1] T. Aubin, A course in differential geometry, Grad. Stud. Math., vol. 27, Amer. Math. Soc., Providence, RI, 2001.

[2] Y. Bizais (Ed.), Proceedings of the VIIth International Conference on Fully Three-Dimensional Reconstruction in Radiology and Nuclear Medicine, Phys. Medicine Biol. (Special Issue) 49 (2004).

[3] C. Bontus, R. Proksa, J. Timmer, T. Köhler, M. Grass, Movement artifacts in helical CT cone-beam reconstruction, in: R. Huesman (Ed.), Proceedings of the International Meeting on Fully Three-Dimensional Image Reconstruction in Radiology and Nuclear Medicine, Pacific Grove, CA, USA, Oct. 30–Nov. 2, 2001, 2001, pp. 199–202.

[4] C. Bontus, T. Köhler, R. Proksa, A quasiexact reconstruction algorithm for helical CT using a 3-PI acquisition, Medical Phys. 30 (2003) 2493–2502.

[5] P.E. Danielsson, P. Edholm, J. Eriksson, M.M. Seger, Towards exact reconstruction for helical cone-beam scanning of long objects. A new detector arrangement and a new completeness condition, in: D.W. Townsend, P.E. Kinahan (Eds.), Proc. 1997 Meeting on Fully 3D Image Reconstruction in Radiology and Nuclear Medicine, Pittsburgh, 1997, pp. 141–144.

[6] M. Defrise, F. Noo, H. Kudo, A solution to the long-object problem in helical cone-beam tomography, Phys. Medicine Biol. 45 (2000) 623–643.

[7] A. Katsevich, Theoretically exact filtered backprojection-type inversion algorithm for Spiral CT, SIAM J. Appl. Math. 62 (2002) 2012–2026.

[8] A. Katsevich, Analysis of an exact inversion algorithm for spiral cone-beam CT, Phys. Medicine Biol. 47 (2002) 2583–2598.

[9] A. Katsevich, A general scheme for constructing inversion algorithms for cone beam CT, Internat. J. Math. Math. Sci. 21 (2003) 1305–1321.

[10] A. Katsevich, An improved exact filtered backprojection algorithm for spiral computed tomography, Adv. in Appl. Math. 32 (2004) 681–697.

[11] T. Köhler, R. Proksa, C. Bontus, M. Grass, J. Timmer, Artifact analysis of approximate cone-beam CT algorithms, Medical Phys. 29 (2002) 51–64.

[12] T. Köhler, C. Bontus, P. Koken, A new approach to handle redundant data in helical cone-beam CT, in: F. Noo, H. Kudo, L. Zeng (Eds.), Proceedings of the VIIIth International Conference on Fully 3D Reconstruction in Radiology and Nuclear Medicine, University of Utah, Salt Lake City, UT, 2005, online access: http://www.ucair.med.utah.edu/3D05/proceedings.html.

[13] F. Noo, J. Pack, D. Heuscher, Exact helical reconstruction using native cone-beam geometries, Phys. Medicine Biol. 48 (2003) 3787–3818.

[14] F. Noo, H. Kudo, L. Zeng (Eds.), Proceedings of the VIIIth International Conference on Fully Three-Dimensional Reconstruction in Radiology and Nuclear Medicine, University of Utah, Salt Lake City, UT, 2005, online access: http://www.ucair.med.utah.edu/3D05/proceedings.html.

[15] J.D. Pack, F. Noo, R. Clackdoyle, Cone-beam reconstruction using the backprojection of locally filtered projections, IEEE Trans. Medical Imaging 24 (2005) 1–16.
[16] R. Proksa, T. Köhler, M. Grass, J. Timmer, The n-PI method for helical cone-beam CT, IEEE Trans. Medical Imaging 19 (2000) 848–863.
[17] E. Sidky, Y. Zou, X. Pan, Minimum data image reconstruction algorithms with shift-invariant filtering for helical, cone-beam CT, Phys. Medicine Biol. 50 (2005) 1643–1657.
[18] K.C. Tam, S. Samarasekera, F. Sauer, Exact cone beam CT with a spiral scan, Phys. Medicine Biol. 43 (1998) 1015–1024.
[19] Y. Ye, G. Wang, Filtered backprojection formula for exact image reconstruction from cone-beam data along a general scanning curve, Medical Phys. 32 (2005) 42–48.
[20] H. Yu, Y. Ye, S. Zhao, G. Wang, A backprojection-filtration algorithm for nonstandard spiral cone-beam CT with an n-PI-window, Phys. Medicine Biol. 50 (2005) 2099–2111.
[21] T. Zhuang, S. Leng, B.E. Nett, G. Chen, Fan-beam and cone-beam image reconstruction via filtering the backprojection image of differentiated projection data, Phys. Medicine Biol. 49 (2004) 1643–1657.
[22] T. Zhuang, B.E. Nett, S. Leng, G. Chen, A shift-invariant FBP image reconstruction algorithm with variable data usage for helical cone-beam CT, in: F. Noo, H. Kudo, L. Zeng (Eds.), Proceedings of the VIIIth International Conference on Fully 3D Reconstruction in Radiology and Nuclear Medicine, University of Utah, Salt Lake City, UT, 2005, online access: http://www.ucair.med.utah.edu/3D05/proceedings.html.
[23] Y. Zou, X. Pan, Exact image reconstruction on PI-lines from minimum data in helical cone-beam CT, Phys. Medicine Biol. 49 (2004) 941–959.